9-16-2016

Dynamics of orographic gravity waves observed in the mesosphere over Auckland Islands during the Deep Propagating Gravity Wave Experiment (DEEPWAVE)

Stephen D. Eckermann
Space Science Division, U.S. Naval Research Laboratory, Washington, D.C.

Dave Broutman
Computational Physics, Inc.

Jun Ma
Computational Physics, Inc.

James D. Doyle
Marine Meteorology Division, U.S. Naval Research Laboratory, Monterey, California

Pierre-Dominique Pautet
Utah State University, dominiquepautet@gmail.com

Michael J. Taylor
Utah State University, mike.taylor@usu.edu

See next page for additional authors

Recommended Citation
Eckermann S.D., Broutman D., Ma J., Doyle J.D., Pautet P.-D., Taylor M.J., Bossert K., Williams B.P., Fritts D.C., and Smith R.B., Dynamics of orographic gravity waves observed in the mesosphere over Auckland Islands during the Deep Propagating Gravity Wave Experiment (DEEPWAVE), J. Atmos. Sci., doi: 10.1175/JAS-D-16-0059.1, 2016

Dynamics of Orographic Gravity Waves Observed in the Mesosphere over the Auckland Islands during the Deep Propagating Gravity Wave Experiment (DEEPWAVE)

STEPHEN D. ECKERMANN,[a] DAVE BROUTMAN,[b] JUN MA,[b] JAMES D. DOYLE,[c] PIERRE-DOMINIQUE PAUTET,[d] MICHAEL J. TAYLOR,[d] KATRINA BOSSERT,[e] BIFFORD P. WILLIAMS,[e] DAVID C. FRITTS,[e] AND RONALD B. SMITH[f]

[a] *Space Science Division, U.S. Naval Research Laboratory, Washington, D.C.*
[b] *Computational Physics, Inc., Springfield, Virginia*
[c] *Marine Meteorology Division, U.S. Naval Research Laboratory, Monterey, California*
[d] *Center for Atmospheric and Space Sciences, Utah State University, Logan, Utah*
[e] *GATS, Inc., Boulder, Colorado*
[f] *Department of Geology and Geophysics, Yale University, New Haven, Connecticut*

(Manuscript received 22 February 2016, in final form 2 June 2016)

ABSTRACT

On 14 July 2014 during the Deep Propagating Gravity Wave Experiment (DEEPWAVE), aircraft remote sensing instruments detected large-amplitude gravity wave oscillations within mesospheric airglow and sodium layers at altitudes $z \sim 78$–83 km downstream of the Auckland Islands, located ~1000 km south of Christchurch, New Zealand. A high-altitude reanalysis and a three-dimensional Fourier gravity wave model are used to investigate the dynamics of this event. At 0700 UTC when the first observations were made, surface flow across the islands' terrain generated linear three-dimensional wave fields that propagated rapidly to $z \sim 78$ km, where intense breaking occurred in a narrow layer beneath a zero-wind region at $z \sim 83$ km. In the following hours, the altitude of weak winds descended under the influence of a large-amplitude migrating semidiurnal tide, leading to intense breaking of these wave fields in subsequent observations starting at 1000 UTC. The linear Fourier model constrained by upstream reanalysis reproduces the salient aspects of observed wave fields, including horizontal wavelengths, phase orientations, temperature and vertical displacement amplitudes, heights and locations of incipient wave breaking, and momentum fluxes. Wave breaking has huge effects on local circulations, with inferred layer-averaged westward flow accelerations of ~350 m s^{-1} h^{-1} and dynamical heating rates of ~8 K h^{-1}, supporting recent speculation of important impacts of orographic gravity waves from subantarctic islands on the mean circulation and climate of the middle atmosphere during austral winter.

1. Introduction

The Deep Propagating Gravity Wave Experiment (DEEPWAVE) was a field measurement campaign to observe the end-to-end dynamics of gravity waves—generation, propagation, breakdown, and effects on large-scale circulations—at altitudes from the ground to ~100 km. The primary observational platform was the National Science Foundation (NSF)/National Center for Atmospheric Research (NCAR) Gulfstream V research aircraft (NGV: Laursen et al. 2006), which for DEEPWAVE was equipped with a suite of in situ and remote sensing instruments to observe gravity wave dynamics over this deep altitude range. The field phase of DEEPWAVE took place from May to July 2014 from an operating base in Christchurch, New Zealand, which provided regular NGV access to major orographic and nonorographic sources of gravity waves, while the strong vortex-edge winds in austral winter provided a stable propagation channel for deep propagation of these waves into the mesosphere and lower thermosphere (MLT). Fritts et al. (2016) review the planning, execution, and initial results of DEEPWAVE.

One of the many scientific objectives of DEEPWAVE was to acquire gravity wave observations to test recent ideas that gravity waves generated by small island

Corresponding author address: Stephen Eckermann, Code 7631, Geospace Science and Technology Branch, Space Science Division, U.S. Naval Research Laboratory, 4555 Overlook Avenue SW, Washington, DC 20375.
E-mail: stephen.eckermann@nrl.navy.mil

DOI: 10.1175/JAS-D-16-0059.1

terrain in the Southern Ocean significantly influence the large-scale momentum budget of the middle atmosphere in austral winter. This idea first arose when Alexander et al. (2009) analyzed radiances acquired by the Atmospheric Infrared Sounder (AIRS) on the *Aqua* satellite in September 2003 and found three-dimensional gravity waves in the upper stratosphere emanating from the small subantarctic island of South Georgia. Alexander et al. (2009) inferred significant momentum flux deposition from these waves and, since global models typically treat grid cells containing small islands as ocean rather than land, they speculated that omission of gravity wave drag from small subantarctic islands might explain some or all of the stratospheric "cold pole" bias in global models during austral winter (Butchart et al. 2011).

McLandress et al. (2012) tested this idea by inserting artificial subgrid-scale orography into their model's orographic gravity wave drag parameterization near 60°S. This small change substantially reduced the model's cold-pole bias in austral winter but somewhat degraded its ozone simulations. Alexander and Grimsdell (2013) later extended the AIRS analysis to other subantarctic islands and different austral winters, finding deep gravity waves to be common over many of the islands they studied, and that estimated wave momentum fluxes could explain some, but perhaps not all, of the cold-pole drag deficit inferred from modeling studies such as McLandress et al. (2012).

Nadir satellite imagers such as AIRS currently provide the only routine observations of deep gravity wave activity from these remote islands. Unfortunately these gravity wave perturbations occur near (and in some cases beyond) the resolution and noise limits of the sensor, so our knowledge of deep gravity wave dynamics over islands remains fragmented. Likewise, global models cannot resolve these waves and presently resort to simple augmentations to existing parameterizations to assess potential effects (McLandress et al. 2012). More recently, high-resolution linear and nonlinear models have been used to model orographic gravity waves from South Georgia, revealing deep propagation of waves into the stratosphere and drag effects due to wave breaking on the stratospheric circulation (Jiang et al. 2014; Vosper 2015). However, similarly extensive high-resolution observations of these island wave fields were not available to validate these simulations.

DEEPWAVE provided an opportunity to use the instrumented NGV to acquire detailed observations of deep gravity wave dynamics over subantarctic islands for the first time and potentially to higher altitudes. Thus, ahead of the mission, islands south of New Zealand were studied as potential measurement candidates. The Auckland Island archipelago received particular scrutiny, because, as shown in Fig. 1, it is located ~1000 km south-southwest of Christchurch, well within flight range of the NGV, and is

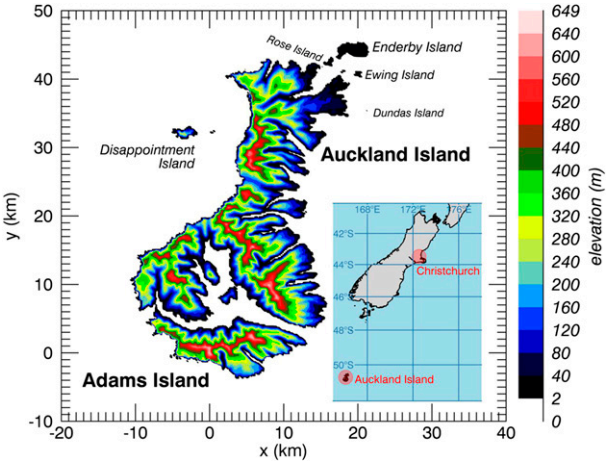

FIG. 1. Terrain elevations $h(x, y)$ of the Auckland Island archipelago derived from ASTER observations (see section 2c). Origin of (x, y) coordinate axes is located at Mount Dick, the highest peak. (inset) Map showing location of Auckland Island relative to DEEPWAVE operating base in Christchurch, New Zealand.

lined by significant mountain ranges with individual peaks over 600 m high. For simplicity, in this paper we will refer to all the islands of this archipelago, including Auckland Island, Adams Island, and surrounding islets depicted in Fig. 1, collectively as "Auckland Island."

The AIRS analysis of Alexander and Grimsdell (2013) was unable to distinguish gravity waves emanating from Auckland Island and southern New Zealand, raising doubts about whether Auckland Island produced any deep gravity wave activity to observe. Thus, ahead of DEEPWAVE a 9-yr climatology of stratospheric gravity wave amplitudes over the greater New Zealand region was recomputed from AIRS data using modified analysis and averaging algorithms and a different collection of AIRS thermal radiance channels to improve signal to noise and geographical resolution [following Eckermann and Wu (2012) and Eckermann et al. (2016b, unpublished manuscript)]. The resulting variance maps, shown in Fig. 1a of Fritts et al. (2016), revealed a small but statistically significant peak in AIRS variances immediately downstream of Auckland Island that was distinct from larger peaks observed near New Zealand, identifying Auckland Island as a source of deep gravity wave activity and thus a viable measurement target for the NGV during DEEPWAVE.

On 14 July 2014, DEEPWAVE NGV research flight number 23 (RF23) overflew Auckland Island on four separate occasions and observed orographic gravity waves in the MLT downstream of the island terrain (Fritts et al. 2016; Pautet et al. 2016). Here we conduct a detailed investigation of the dynamics of these observed wave fields. Section 2 reviews the RF23 flight plan, the NGV instruments that observed the MLT, and a 0–100-km

DEEPWAVE reanalysis, which provides backgrounds for a Fourier model for computing three-dimensional linear orographic gravity wave solutions. In section 3 we investigate the dynamics of MLT wave fields observed during the outbound flight leg at ~0700 UTC. Section 4 focuses on the time evolution of winds and waves in the MLT over Auckland Island during the ~7-h duration of the flight, particularly the influence of a large-amplitude semidiurnal tide in the MLT reanalysis. This provides context for our investigation in section 5 of observed wave field dynamics during the inbound flight legs that occurred ~3–4 h after the initial outbound observations. In section 6 we review our findings and methods, then assess broader ramifications of these observed wave fields for the momentum and energy budgets of the middle atmosphere.

2. Observations, analysis, and modeling tools

a. *DEEPWAVE RF23 observations*

1) FLIGHT PLAN

Fritts et al. (2016) review the numerical weather prediction (NWP) models and ancillary tools used to inform DEEPWAVE flight planning. In the days prior to 14 July 2014, the NWP models predicted southwesterly near-surface flow upstream of Auckland Island intensifying to ~20 m s^{-1} (see Fig. 2), with wind speeds increasing with height into a strong southwesterly tropospheric jet. High-resolution regional forecasts centered over Auckland Island using the U.S. Naval Research Laboratory (NRL) Coupled Ocean–Atmosphere Mesoscale Prediction System (COAMPS: Hodur 1997; Doyle et al. 2011) and Mountain Wave Forecast Model (Eckermann et al. 2006b) predicted wave generation and penetration of orographic gravity waves into the stratosphere.

Accordingly, the RF23 flight track was devised, among other things, to profile possible deep orographic gravity waves over Auckland Island. Figure 3 provides a three-dimensional representation of the flight track executed by the NGV. After taking off from Christchurch at 0545 UTC and flying south at 40 kft (12.2 km), the first transect of Auckland Island occurred from 0650 to 0715 UTC at ~12-km altitude. The first dropsonde (D1) was deployed from the NGV at 0713 UTC to measure the upstream atmospheric environment using the Airborne Vertical Atmospheric Profiling System (AVAPS; Young et al. 2014). Thereafter the NGV flew southwest to Macquarie Island (not shown), before returning to Auckland Island ~3 h later and performing three more transects of the island, first at ~4 km, then at ~7.5 km, and finally at ~12 km, with two additional dropsondes deployed upstream and downstream. Figure 2b reveals that (as planned) NGV transects across Auckland Island were close to parallel to the forecast upstream surface flow.

2) MLT OBSERVATIONS

Gravity waves were observed in the MLT near Auckland Island using two remote sensing instruments on board the NGV. Fritts et al. (2016) and Pautet et al. (2016) review this instrumentation and the MLT gravity wave measurements during RF23, and so only a brief summary is provided here. Later sections investigate the observed MLT gravity wave characteristics in detail.

The Advanced Mesospheric Temperature Mapper (AMTM) measured the temperature-sensitive infrared (3, 1) Meinel band of hydroxyl, which during RF23 emitted from a 7–8-km-thick mesospheric layer peaking at a height $z \sim 83.5$ km (Pautet et al. 2016). Rotational temperatures were retrieved from airglow brightness acquired by a zenith-viewing imager using the algorithms set forth in Pautet et al. (2014). Two additional "wing" cameras imaged airglow brightness on either side of the aircraft: although temperatures were not retrieved from these observations, for simplicity we refer to all three imagers collectively as the AMTM from this point forward. MLT sodium (Na) abundances were also measured from the NGV using a zenith-pointing 589-nm lidar. Additional details on this lidar system can be found in Bossert et al. (2015).

b. *NAVGEM reanalysis*

To model the evolution and dynamics of gravity waves observed in the MLT during RF23, accurate wind and temperature profiles are needed from the surface to the MLT upstream of Auckland Island. Global analyses issued by operational centers provide the best estimates of local winds and temperatures owing to their assimilation of available observations, which near Auckland Island come from satellite overpasses in addition to the three NGV AVAPS profiles (see below). These production data assimilation (DA) systems currently extend only to ~50–70-km altitude, leaving a critical analysis gap from ~60 to 100 km, where waves can be significantly refracted, filtered, or dissipated.

Thus, a 0–100-km reanalysis project for the entire DEEPWAVE austral winter was undertaken using a high-altitude configuration of the Navy Global Environmental Model (NAVGEM). This system and its DEEPWAVE reanalysis products are the subject of a separate paper (Eckermann et al. 2016a, unpublished manuscript), and so only a brief overview relevant to the current study is provided here. NAVGEM is the U.S. Navy's operational global NWP system, comprising a forecast model based on a 3-time-level semi-implicit

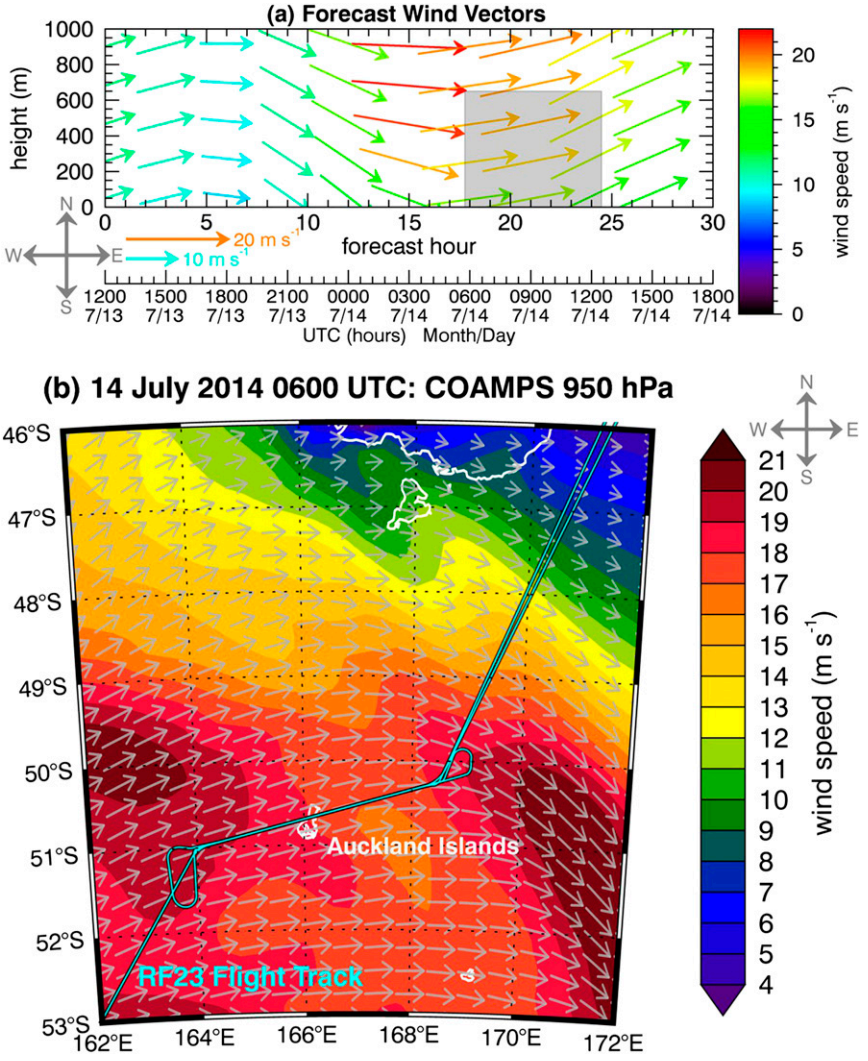

FIG. 2. (a) Time evolution of horizontal wind vectors in lowest kilometer of the atmosphere upstream of Auckland Island (50.5°–51°S, 165°–166°E) as forecast by the NCEP Global Forecast System initialized at 1200 UTC 13 Jul 2014. Gray region shows time period of RF23 and peak height of Auckland Island terrain (h_{peak} = 650 m). (b) +18 h COAMPS forecasts, initialized at 1200 UTC 13 Jul 2014 (valid at 0600 UTC 14 Jul), of 950-hPa horizontal wind speeds (shaded; color bar indicates scale and units). Corresponding horizontal wind vectors are depicted in gray. Aqua curve shows NGV flight track during RF23.

semi-Lagrangian discretization of the fluid equations on the sphere, coupled to a four-dimensional variational (4DVAR) DA algorithm. Hogan et al. (2014) provide a detailed description of the key model and DA components.

In common with other operational DA systems, the current operational NAVGEM has a rigid upper boundary at 0.04 hPa ($z \sim 70$ km: Hogan et al. 2014). For the DEEPWAVE reanalysis, the forecast model was reconfigured from 60 to 74 levels (L74) with a new upper boundary at 6×10^{-5} hPa ($z \sim 115$ km), then augmented with a range of additional physical parameterizations needed to model the MLT. The DA system continued to assimilate its regular extensive suite of archived operationally available observations spanning the 0–50-km-altitude range. Among these were the AVAPS dropsonde data that, after rapid postprocessing in Christchurch, were transmitted on WMO's Global Telecommunication System (GTS) for access by operational centers. From 50 to 100 km, the system assimilated the following additional observations:

1) temperature-sensitive microwave radiances from the upper-atmosphere sounding (UAS) channels of the

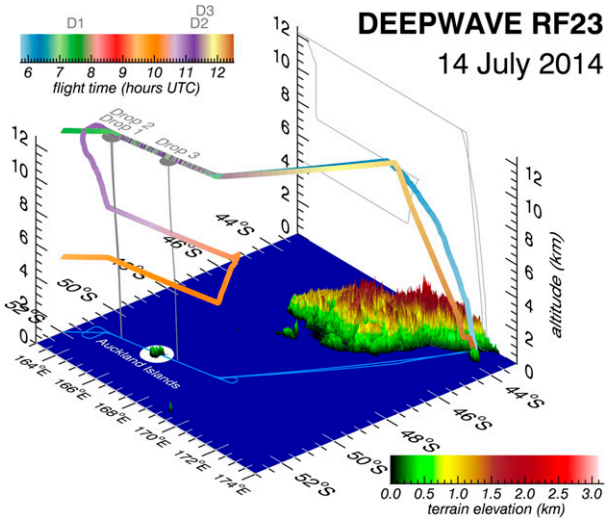

FIG. 3. Three-dimensional depiction of part of the NGV flight track during RF23, with colors along track depicting time (UTC hours; color bar at top left). Flight track from ~0724 to 0933 UTC to/from Macquarie Island lies outside the plot boundary to the southwest. Blue curve on ocean surface shows NGV ground track (as in Fig. 2b), showing repeated transects across Auckland Island, spotlighted in white. Terrain elevations over Auckland Island and New Zealand are shown in color bar at bottom right. Light gray curves at 43°S show latitude–height projection of flight track, revealing stair-step transects across Auckland Island on inbound leg at 4-, 7.5-, and 12-km altitude. Dark gray circles show locations of three AVAPS dropsonde releases from the NGV, gray curves beneath show descent trajectories, and release times are depicted as D1, D2, and D3 in color bar at top left.

Special Sensor Microwave Imager/Sounder (SSMIS) on four Defense Meteorological Satellite Program (DMSP) polar orbiters (F16–F19 inclusive), using the NAVGEM UAS radiance assimilation procedures described in Hoppel et al. (2013);

2) limb measurements of temperature and water vapor up to 0.002 hPa from version 3.3 retrievals of the Microwave Limb Sounder (MLS) on the *Aura* satellite and of temperature up to 10^{-4} hPa from version 2.0 retrievals of the Sounding of the Atmosphere Using Broadband Emission Radiometry (SABER) instrument on the *Thermosphere Ionosphere Mesosphere Energetics and Dynamics* (*TIMED*) satellite, using assimilation procedures for these instruments described in Eckermann et al. (2009).

Static bias correction profiles for MLS and SABER were updated from those in Eckermann et al. (2009) based on mean biases computed for coincident profiles for the period 2004–13 using version 3.3 MLS and version 2.0 SABER temperatures. At heights above 0.002-hPa SABER temperatures were assumed to be unbiased.

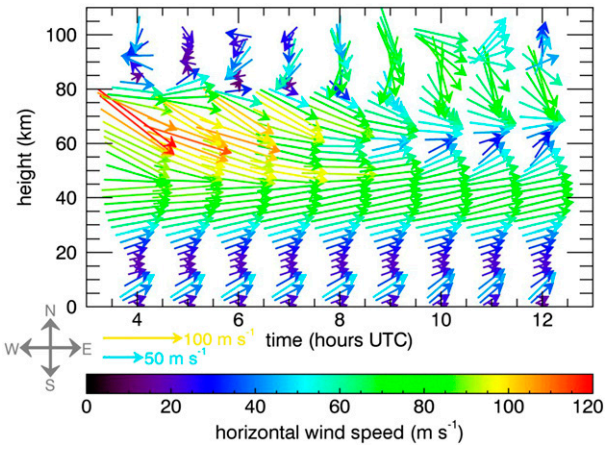

FIG. 4. Horizontal wind vectors upstream of Auckland Island on 14 Jul 2014 from NAVGEM reanalysis, plotted at hourly intervals from 0400 to 1200 UTC over the range z = 0–100 km.

The system was initialized on 23 March 2014, roughly two months prior to the core May–July DEEPWAVE period, and run out to the end of September. The March–April period was treated as a DA spinup phase.

For this study, given the focus on large-scale background conditions controlling wave propagation, we used reanalyses from a low-horizontal-resolution reanalysis run using a T119 forecast model (outer loop) coupled to a T47 tangent linear forecast model (TLM, inner loop) used by the 4DVAR DA algorithm. Comparisons to a companion L74 reanalysis run using T425 outer and T159 inner loops revealed generally close agreement, though with more finescale structure in the T425 analysis at upper levels due to resolved large-scale gravity waves. The reanalyzed winds and temperatures from 0 to 50 km have been compared to other publically available operational analyses and reanalyses, revealing generally close agreement. We expect the NAVGEM 4DVAR DA algorithm to improve MLT tidal assimilation, relative to our earlier high-altitude 3DVAR-based system (Eckermann et al. 2009), by realistically (nonlinearly) propagating MLT increments from the various measurement times to the central analysis time using the TLM. To further improve our representation of MLT tidal effects, the 6-hourly reanalysis fields were filled at intervening hourly intervals using the 1–5-h forecasts from each DA cycle.

Figure 4 displays the NAVGEM reanalyzed horizontal wind vectors $\mathbf{V} = (U, V)$ from z = 0 to 100 km upstream of Auckland Island at hourly intervals from 0400 to 1200 UTC on 14 July, corresponding to the periods just before, during, and just after RF23. Geometric heights z were approximated using the analyzed geopotential height profiles. The profiles reveal strong

westerlies from 0 to 70 km, with surface winds near 20 m s^{-1} increasing to a southwesterly tropospheric jet peaking in excess of 50 m s^{-1} near 7 km. At 0400–0500 UTC just prior to RF23, the stratopause jet peaked at over 100 m s^{-1} near 70 km, with rapid diminution of wind speeds above this level due to gravity wave drag. The peak stratopause winds over the island progressively weakened over the next 6–8 h. A detailed analysis of the MLT wind fields is provided in section 4a.

c. *Fourier gravity wave model*

To model the observed MLT gravity waves, we use a Fourier method that has proven well suited to modeling stationary three-dimensional orographic gravity waves observed over islands: the method was used previously to model three-dimensional orographic wave fields observed in the stratosphere over South Georgia (Alexander et al. 2009; Jiang et al. 2014) and in the troposphere downstream of Jan Mayen (Eckermann et al. 2006a). Preliminary Fourier solutions also revealed striking similarities with the MLT gravity waves observed during RF23 (Fritts et al. 2016; Pautet et al. 2016), motivating a more detailed modeling effort here.

We consider linear nonhydrostatic stationary gravity waves in a height-dependent background atmosphere. For a wavenumber vector (k, l, m) and background wind profile $\mathbf{V}(z) = (U, V)$, the intrinsic frequency $\breve{\omega}(k, l, z) = -kU(z) - lV(z)$. The nonhydrostatic irrotational gravity wave dispersion relation gives the corresponding vertical wavenumber

$$m(k,l,z) = sk_h\left(\frac{N^2}{\breve{\omega}^2} - 1\right)^{1/2}, \tag{1}$$

where $N(z)$ is the background buoyancy frequency profile, $k_h^2 = k^2 + l^2$, and the sign parameter

$$s(k,l) = -\text{sign}[\breve{\omega}(k,l,0)] \tag{2}$$

ensures upward group propagation ($c_{gz} = \partial\breve{\omega}/\partial m > 0$) for each Fourier component.

We express wave field perturbations of a given atmospheric parameter X as the inverse Fourier transform

$$X(x,y,z) = \int\int_{-\infty}^{\infty} S(k,l,z)\tilde{X}(k,l,z)e^{i(kx+ly)}\,dk\,dl. \tag{3}$$

A filter function $S(k, l, z)$ is inserted here for later use: until otherwise noted, $S(k, l, z) = 1$.

We evaluate (3) numerically by computing the Fourier solution $\tilde{X}(k, l, z)$ using ray methods, then performing a two-dimensional fast inverse Fourier transform at each height z. Although our full Fourier ray solution includes vertical reflections, resonant modes, and evanescent tunneling (e.g., Eckermann et al. 2006a; Broutman et al. 2006, 2009), here we omit those terms since our primary focus in this paper is propagating waves that reach the MLT. Thus at the surface we initialize only those Fourier components $\tilde{X}(k, l, 0)$ that are propagating (i.e., $m^2 > 0$ at $z = 0$). As z increases, many of these initially propagating Fourier components become nonpropagating by reaching either a turning point z_{tp}, where $m^2(k, l, z_{tp}) \to 0$ ($\breve{\omega}^2 \to N^2$), or a critical level z_{cl}, where $m^2(k, l, z_{cl}) \to \infty$ ($\breve{\omega}^2 \to 0$). Again we simply remove those Fourier components at $z \geq z_{tp}$ and $z \geq z_{cl}$ and ignore downward-propagating waves due to reflection at $z = z_{tp}$.

With these simplifications, the ray solution for vertical displacement η is

$$\tilde{\eta}(k,l,z) = \left[\frac{\rho_0}{\rho(z)}\right]^{1/2}\tilde{h}g\,\exp\left(i\int_0^z m\,dz\right), \tag{4}$$

where $\rho(z)$ is background air density, ρ_0 is the upstream value at $z = 0$,

$$g(k,l,z) = \left[\frac{c_{gz}(k,l,0)N^2(0)\breve{\omega}(k,l,z)}{c_{gz}(k,l,z)N^2(z)\breve{\omega}(k,l,0)}\right]^{1/2} \tag{5}$$

is a wave-action conservation term [cf. Eq. (22) of Eckermann et al. (2015b)], and $\tilde{h}(k, l)$ is the Fourier transform of the terrain heights $h(x, y)$. The latter defines the equivalent Fourier form

$$\tilde{\eta}(k,l,0) = \tilde{h}(k,l) \tag{6}$$

of the linear lower boundary condition $\eta(x, y, 0) = h(x, y)$. Solutions for other variables X follow from polarization relations (see examples below).

Although the Fourier solution $\tilde{X}(k, l, z)$ represents only the steady-state ($t \to \infty$) wave field, we can use these solutions to approximate time-evolving wave fields typical of an initial value problem with "switch on" of surface forcing at $t = 0$. Since each harmonic (k, l) has an associated group propagation time

$$t_{\text{prop}}(k,l,z) = \int_0^z c_{gz}^{-1}(k,l,z')\,dz' \tag{7}$$

to reach a given height z, then imposing a fixed cutoff time limit $t_{\text{prop}}(k, l, z_c) = t_c$ and solving numerically for z in (7) yields a spectrum of corresponding cutoff altitudes $z_c(k, l, t_c)$. We can use this result to approximate the time-dependent wave field solution $X(x, y, z, t)$ at time $t = t_c$ using the inverse Fourier transform (3), as before, but applying a time-dependent filter function S of the form

$$S_{\text{prop}}(k,l,z,t)=\begin{cases}1 & z\le z_c(k,l,t)[t_{\text{prop}}(k,l,z)\le t]\\ 0 & z>z_c(k,l,t)[t_{\text{prop}}(k,l,z)>t],\end{cases} \quad (8)$$

for any specified $t = t_c$. Broutman et al. (2006) used a very similar method to model evolution of trapped orographic gravity waves, finding close agreement with direct numerical simulations.

For direct comparisons with the RF23 MLT observations, we convert wave field solutions for vertical displacment $\eta(x, y, z, t)$ into perturbation temperatures using the adiabatic relation (e.g., Eckermann et al. 1998)

$$T'=-\left(\frac{\overline{T}N^2}{g}\right)\eta, \quad (9)$$

where g is gravitational acceleration and $\overline{T}(z)$ is the background temperature profile. We also present solutions for wave steepness η_z, defined as the vertical derivative of η and given by the Fourier integral

$$\eta_z(x,y,z,t)=\int\int_{-\infty}^{\infty} im\,S_{\text{prop}}\tilde{\eta}e^{i(kx+ly)}\,dk\,dl. \quad (10)$$

We use these solutions to check for linearity ($\eta_z < 1$) and to diagnose transition to wavebreaking amplitudes ($\eta_z > 1$) versus height and time in the MLT. We do not attempt to parameterize the net nonlinear effects of wave breaking on modeled wave fields.

We derive vertical fluxes of horizontal momentum per unit mass using the Fourier solutions for wave-induced vector velocity derived from polarization relations: first, vertical velocity $\tilde{w}=-i\,\tilde{\omega}\,\tilde{\eta}$, then zonal and meridional velocities $\tilde{u}=-kmk_h^{-2}\tilde{w}$ and $\tilde{v}=-lmk_h^{-2}\tilde{w}$, respectively. Given a Fourier ray solution $\tilde{X}(k, l, z)$ in any atmospheric parameter X, we can derive a corresponding complex wave field solution

$$\mathring{X}(x,y,z,t)=X_A(x,y,z,t)e^{i\psi_X(x,y,z,t)}, \quad (11)$$

where X_A is local wave amplitude and ψ_X is local phase, using

$$\mathring{S}(k,l)=1-s(k,l), \quad (12)$$

multiplied by S_{prop} in (8) for the filter function S in (3), where $s(k, l)$ is as defined in (2). In this way we use our Fourier vector velocity solutions $(\tilde{u}, \tilde{v}, \tilde{w})$ to derive complex wave field velocities $(\mathring{u}, \mathring{v}, \mathring{w})$, which we combine to yield the vertical fluxes of zonal and meridional momentum flux per unit mass

$$\overline{uw}(x,y,z,t)=\frac{1}{4}(\mathring{u}\mathring{w}^*+\mathring{u}^*\mathring{w}) \quad \text{and} \quad (13)$$

$$\overline{vw}(x,y,z,t)=\frac{1}{4}(\mathring{v}\mathring{w}^*+\mathring{v}^*\mathring{w}), \quad (14)$$

respectively, where asterisks denote complex conjugation (Eckermann et al. 2010).

All Fourier solutions to follow were computed within an $(n_x\Delta x, n_y\Delta y, n_z\Delta z)$ domain with $n_x = n_y = 4096$, $n_z = 201$, $\Delta x = \Delta y = 1$ km, and $\Delta z = 500$ m. A small amount of vertical diffusive damping ($K_{zz} = 1\,\text{m}^2\,\text{s}^{-1}$) was used to avoid wraparound interference in the solutions (see appendix A of Eckermann et al. 2015b). In specifying terrain elevations $h(x, y)$ for Auckland Island at the model's lower boundary, we encountered considerable disagreement among some commonly used digital terrain databases, which our Fourier solutions proved sensitive to. The terrain adopted in this study, plotted in Fig. 1, was obtained at 200-m horizontal resolution from a global digital elevation model derived from measurements by the Advanced Spaceborne Thermal Emission and Reflection Radiometer (ASTER) on NASA's *Terra* satellite then reinterpolated onto the model's $1 \times 1\,\text{km}^2$ horizontal grid.

3. Outbound NGV flight leg

a. Observations

Figure 5a shows the combined OH airglow brightness imagery observed by the AMTM in the MLT during the outbound transect of Auckland Island at ~0700 UTC. Large-amplitude wavelike banding of airglow brightness downstream of Auckland Island is evident. Rotational temperatures retrieved from the zenith camera observations in Fig. 5b reveal oscillations immediately downstream of Auckland Island with a horizontal wavelength $\lambda_h \sim 40$ km and amplitude $\hat{T}_{\text{AG}} \sim 10$ K (Pautet et al. 2016). For a three-dimensional wave field $T'(x, y, z)$, these two-dimensional airglow-derived temperature perturbations can be modeled as

$$T'_{\text{AG}}(x,y)=\int I(z')T'(x,y,z')\,dz'\Big/\int I(z')\,dz', \quad (15)$$

where $I(z)$ is the vertical variation in airglow radiance intensity through the MLT (Liu and Swenson 2003; Fritts et al. 2014). Using a standard Gaussian fit for $I(z)$, during RF23 Pautet et al. (2016) inferred a peak at $z \sim 83.5$ km and a full-width half maximum $\sigma_{z_{\text{AG}}} \sim 7.5$ km. If the wave has a constant amplitude $\hat{T}$ and vertical wavenumber m within the airglow layer, then (15) implies

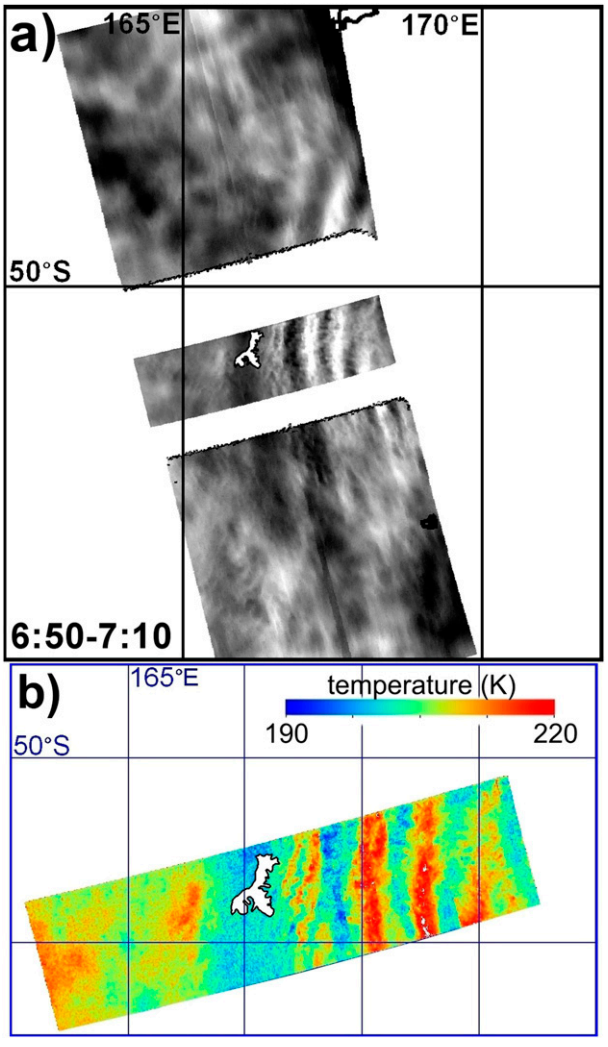

FIG. 5. (a) OH airglow brightness from the AMTM zenith and wing cameras during the first outbound NGV transect. Auckland Island is shaded white with the coastline outlined in black. Time span of these observations (UTC) is indicated at bottom left of this panel. (b) Rotational temperatures retrieved from the zenith camera airglow brightness in (a). See text and Pautet et al. (2016) for further details.

$$\hat{T} = S_{\mathrm{AG}}\hat{T}_{\mathrm{AG}}, \tag{16}$$

where

$$S_{\mathrm{AG}}(m) = \exp(-0.0902\, m^2\, \sigma^2_{z_{\mathrm{AG}}}) \tag{17}$$

(Fritts et al. 2014). Equations (16) and (17) show that in all likelihood the true wave temperature amplitude $\hat{T} \gg \hat{T}_{\mathrm{AG}} = 10\,\mathrm{K}$, with the actual value depending on the wave's vertical wavelength $\lambda_z = 2\pi/|m|$ within the layer.

The minimum vertical wavelength $\lambda_{z_{\mathrm{min}}}$ detectable by the AMTM is ~10 km owing to the finite vertical width $\sigma_{z_{\mathrm{AG}}}$ of the emission layer (Liu and Swenson 2003). Rearranging the dispersion relation (1) to yield $\breve{\omega}^2_{\mathrm{min}}/N^2 = k_h^2/(k_h^2 + m^2_{\mathrm{max}})$, then substituting $k_h = 2\pi\,(40\,\mathrm{km})^{-1}$ and $|m_{\mathrm{max}}| = 2\pi/\lambda_{z_{\mathrm{min}}}$ yields a minimum intrinsic frequency for the wave of $|\breve{\omega}_{\mathrm{min}}| \sim N/4$, so that $N/4 \lesssim |\breve{\omega}| < N$. Thus the wave field here is nonhydrostatic, consistent with the observed downstream penetration of wave activity in Fig. 5b.

Figure 6 shows the Na mixing ratios that were observed in the MLT by the lidar as the NGV approached the island from the east. The observations end just after 0700 UTC as a result of a laser locking problem. Modeling by Xu et al. (2006) shows that, while chemistry becomes important on the bottom side of the Na layer, sodium remains an accurate dynamical tracer of gravity wave motion at these altitudes so long as mixing ratios rather than Na densities are analyzed. In particular, they showed that overturning of Na mixing ratio isopleths on the bottom side of the layer provides a reliable diagnostic of isentropic overturning due to gravity wave breaking, much like a dye tracer in a laboratory tank experiment.

The Na isopleths in Fig. 6 reveal a large-amplitude wave oscillation of ~40-km horizontal wavelength on the bottom side of the Na layer, with overturning clearly evident at 78–80 km at 0700 UTC, or ~30–40 km downstream of the island. The AMTM temperature map in Fig. 5b also shows small-scale instability structures within a primary $\lambda_h \sim 40\,\mathrm{km}$ wave, as typically occurs during incipient wave breaking (e.g., Andreassen et al. 1998), in a region located ~30–40 km downstream of the island. The steep forward face and rapid reduction in wave amplitude in Fig. 6 resemble tropospheric models of three-dimensional orographic gravity wave breaking in the approach to a critical layer (e.g., Miranda and Valente 1997), but in this case ~80 km above the parent terrain. Our modeling in later sections confirms this initial visual impression.

The Na isopleths permit estimates of wave amplitude $\hat{T}$ and vertical wavelength λ_z. Tracking the lowest white isopleth along the x axis of Fig. 6 reveals an unperturbed equilibrium altitude of ~77–78 km and a peak upward displacement to ~81 km near 0700 UTC, implying a maximum vertical displacement amplitude $\hat{\eta} = 3$–4 km. Inserting $\overline{T} = 210$–230 K and $N \sim 0.015$–$0.018\,\mathrm{s}^{-1}$ at 78 km, estimated from NAVGEM reanalysis profiles, into (9) yields $\hat{T} \sim 18$–28 K.

In linear theory, waves become statically unstable and break when the steepness amplitude

$$\hat{\eta}_z = |m|\hat{\eta} \gtrsim 1, \tag{18}$$

so that the maximum wave amplitude at this wave-breaking threshold is

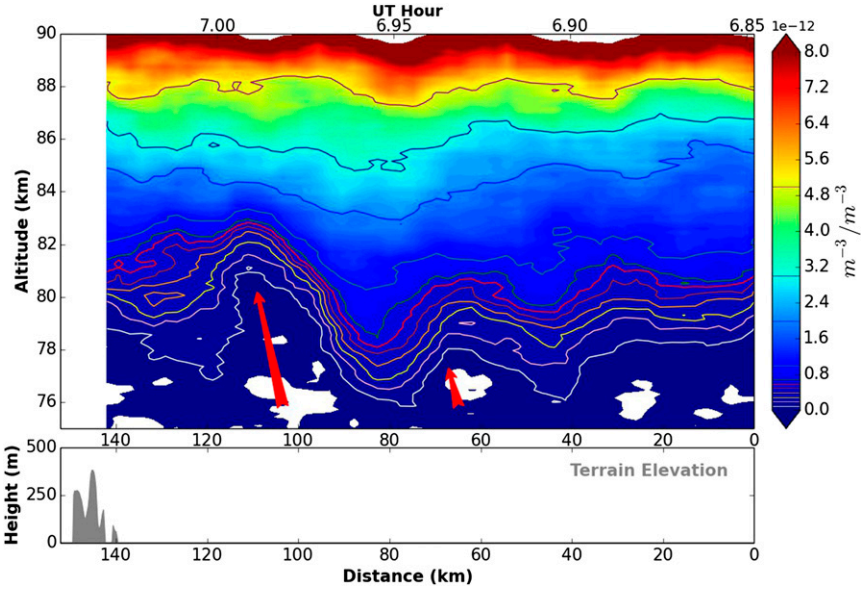

FIG. 6. (top) Na mixing ratios (color bar scale on right indicates units and values of contour line isopleths) observed from 0651 to 0702 UTC 14 Jul 2014 by NGV lidar during approach to Auckland Island; (bottom) the terrain cross section is also shown. Red vertical arrows point to wave crests in vertical displacement 40 km apart, with overturning evident in the larger crest closest to island. White shaded areas denote missing data.

$$\hat{\eta}_{\max} \sim \frac{1}{|m|} \sim \frac{\lambda_z}{2\pi}. \tag{19}$$

Since instability in Fig. 6 occurs at $\hat{\eta} \sim 3$–4 km, (19) suggests $\lambda_z \sim 18$–25 km. Substituting this into (17) yields $S_{\mathrm{AG}} \sim 0.5$–0.7, which, when inserted into (16), yields $\hat{T} \sim 15$–20 K using $\hat{T}_{\mathrm{AG}} \sim 10$ K. This amplitude is somewhat lower than the $\hat{T} \sim 18$–28 K inferred from the Na isopleth displacement, but recall (17) is derived assuming constant $\hat{T}$ and m through the airglow layer, whereas observations in Fig. 6 (as well as later model results) indicate strong vertical gradients in $\hat{T}$ and λ_z as both reduce with height toward a possible overlying critical level.

b. Fourier solutions

To assess linear limits required for application of our Fourier solutions to RF23 wave fields, we first tested the linear lower boundary condition [(6)] by computing the surface Froude number

$$\mathrm{Fr} = \frac{[U^2(0) + V^2(0)]^{1/2}}{N(0)h_{\mathrm{peak}}}. \tag{20}$$

Surface forcing is linear if $\mathrm{Fr} \gtrsim \mathrm{Fr}_c \sim 1$ (where Fr_c is the critical Froude number of ~1) (Smith 1989). Evaluating (20) using analysis fields and RF23 dropsonde data upstream of Auckland Island using $h_{\mathrm{peak}} = 649$ m (see Fig. 1) yielded $\mathrm{Fr} \sim 4 \pm 1$ throughout the RF23 period. Modified formulas that account for low-level vertical gradients (Reinecke and Durran 2008) produced similar findings.

Since the surface forcing environment is linear, we computed Fourier wave field solutions from $z = 0$ to 100 km for a range of propagation cutoff times t_c using upstream wind, height, stability, and density profiles from the NAVGEM reanalysis from 0400 to 1200 UTC (see Fig. 4). At every height z, we computed the maximum value

$$\eta_z^{\max}(z, t_c) = \max[\eta_z(x, y, z, t_c)] \tag{21}$$

of the wave field steepness solutions $\eta_z(x, y, z, t_c)$, as well as the locations $[x_{\max}(z), y_{\max}(z)]$ of those maxima.

Figure 7a shows the resulting $\eta_z^{\max}(z, t_c)$ profiles for t_c values ranging from 1 h through to ∞ (steady state) based on the NAVGEM upstream profiles at 0600 UTC. The $\eta_z^{\max}(z, t_c)$ profiles reveal significant wave activity in the MLT within $t_c = 1.5$ h of forcing at the surface, and by $t_c = 4$ h the profile is already close to the steady-state limit. This is consistent with the high intrinsic frequencies (and hence fast vertical group velocities) inferred earlier for these waves.

Figure 7a also reveals $\eta_z^{\max}(z, t_c) \ll 1$ from $z = 0$ to 65 km, implying linear (nonbreaking) gravity wave dynamics throughout this deep atmospheric layer. At $z \sim 67$ km, $\eta_z^{\max}(z, t_c)$ slowly and asymptotically

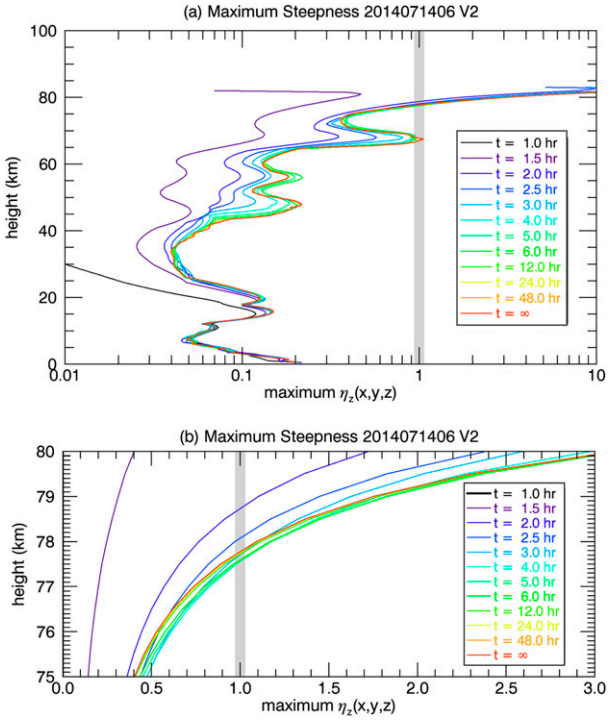

FIG. 7. Vertical profiles of maximum steepness perturbations $\eta_z^{\max}(z, t_c)$ in the 0600 UTC Fourier wave field solutions for cutoff times t_c ranging from 1 h to ∞ (plot legends on right). Results are shown at (a) z = 0–100 km and (b) z = 75–80 km. The wave-breaking threshold $\eta_z = 1$ is marked with a gray line. Abatement of profiles just above 80 km is due to no remaining propagating waves in the solutions.

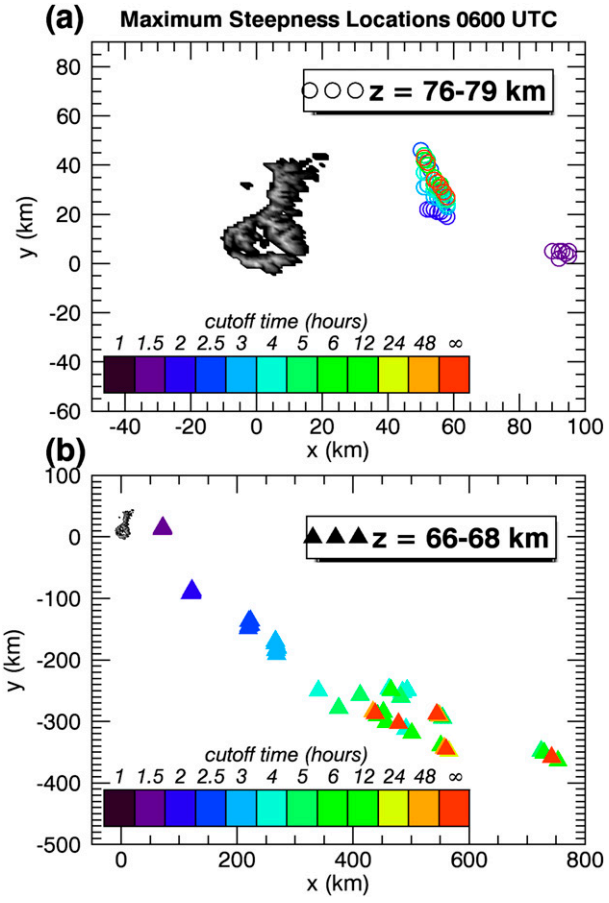

FIG. 8. Locations ($x_{\max}$, $y_{\max}$) of the $\eta_z^{\max}(z, t_c)$ wave field steepness maxima profiled in Fig. 7 at (a) z = 76–79 km (open circles) and (b) z = 66–68 km (filled triangles). The symbol's color in each case depicts the t_c value of the solution (see color bars). Auckland Island terrain on model grid is shown as gray-shaded region.

approaches unity as $t_c \to \infty$, implying a weak slow-developing wave field instability at this altitude. However, as shown in Fig. 8b [see also Broutman et al. (2016), manuscript submitted to *J. Geophys. Res.*], this occurs in a region of the wave field many hundreds of kilometers downstream and to the south of the island, far away from (and hence largely irrelevant to) the wave fields observed in Fig. 5.

Thus, as highlighted in Fig. 7b, the Fourier solutions predict onset of intense wave field instabilities $[\eta_z^{\max}(z, t_c) > 1]$ at a breaking height $z_b \sim 77.5$–78.5 km—exactly the altitude where wave breaking is observed to occur in Fig. 6. Moreover, the corresponding locations $[x_{\max}(z), y_{\max}(z)]$ of maximum wave field instability at these altitudes, plotted in Fig. 8a, all cluster within a tightly confined region ~40 km east of the island, again in agreement with the observed locations of both overturning Na isopleths in Fig. 6 and intrawavelength instability structure in Fig. 5b. Thus, consistent with our diagnostics confirming the validity of linear solutions up to $z \sim 78$ km, those solutions reveal impressive agreement with the salient observed characteristics of the MLT wave fields.

Figure 9a shows the vertical evolution of propagating harmonics in these solutions throughout the stratosphere and MLT. The total number of unique Fourier harmonics is $n_x n_y/2 \approx 8.4 \times 10^6$, yet only ~$10^5$ (or ~1%) of those propagate out of the troposphere, and these are then progressively eroded with height to ~1–2 × 10^4 by $z \sim$ 70–80 km. Some stratospheric filtering occurs as northeastward wind vectors rotate with height to southeastward in Fig. 4, removing horizontal wavenumbers $\mathbf{k}_h = (k, l)$ orthogonal to $\mathbf{V}$ via directional critical-level filtering ($\breve{\omega} = -\mathbf{k}_h \cdot \mathbf{V} \to 0$), as shown in Fig. 9b. Other waves aligned nearly parallel to the intensifying stratospheric winds progressively increase in intrinsic frequency with height, eventually being removed at turning points where $\breve{\omega}^2 \to N^2$ (see Fig. 9c). Figure 9d shows that many waves removed by the cutoff criterion $t > t_c$ for small t_c are eventually removed by critical levels or turning points in the steady-state limit.

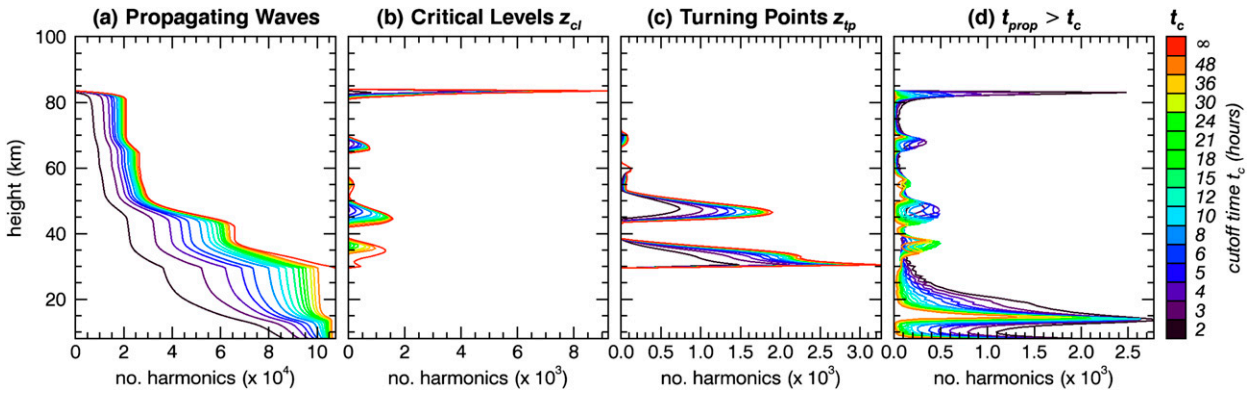

FIG. 9. Spectral filtering of 0600 UTC Fourier solutions vs height for a range of cutoff times t_c depicted by colored curves (color key at far right): (a) number of remaining propagating harmonics (k, l) at each height, and number of harmonics removed at each height by (b) critical levels, (c) turning points, and (d) propagation times $t_{\text{prop}} > t_c$.

Figure 9 also reveals very little wave field filtering above the stratopause jet from $z \sim 55$ to 80 km, but that all remaining waves are removed by critical levels within a narrow layer just above 80 km [accounting also for cessation of $\eta_z^{\max}(z, t_c)$ profiles above ~83 km in Fig. 7a]. This occurs as a result of a rapid reduction in 0600 UTC wind speeds with height in Fig. 4 to a near-zero-wind line at $z \sim 83$ km.

Figure 10 depicts the vertical evolution of these wave field filtering characteristics in spectral space. The lower boundary condition [(6)] of the Fourier $\tilde{\eta}$ solution, $\tilde{h}(k, l)$, is shown in Fig. 10a within a (k, l) spectral range of $\pm 2\pi$ $(10\,\text{km})^{-1}$ where most of the Auckland Island terrain variance is concentrated. Smaller panels to the right depict propagating (red) and nonpropagating (other colors) regions of this spectral space as a function of height within the Fourier solutions at $t_c = 4$ h (top row) and $t_c = \infty$ (bottom row). Comparing the two, we again see that regions where waves are removed by $t > t_c$ cutoffs (black areas) in most cases transition to critical levels or turning points in the steady-state limit.

Below 10 km there are strong northeastward winds and vertical shear (see Fig. 4). The Fourier solutions at $z = 10$ km in Figs. 10b and 10g reveal that **k** vectors orthogonal to those wind vectors have been removed by directional critical-level filtering (green regions), while shorter λ_h waves, particularly those with **k** nearly parallel to the tropospheric wind vectors, have been removed at turning points (blue regions). This leaves a bowtie-shaped wedge of propagating harmonics (red region) at $z = 10$ km that progressively shrinks from $z =$ 10 to 60 km via additional filtering by directional critical levels and turning points, as shown in Figs. 9b and 9c. At $z = 60$ km the remaining propagating waves in Figs. 10c and 10h all have $\lambda_h \gtrsim 30$ km, with the nearly symmetric diamond shape of the propagating (red) region implying a three-dimensional ship-wave response.

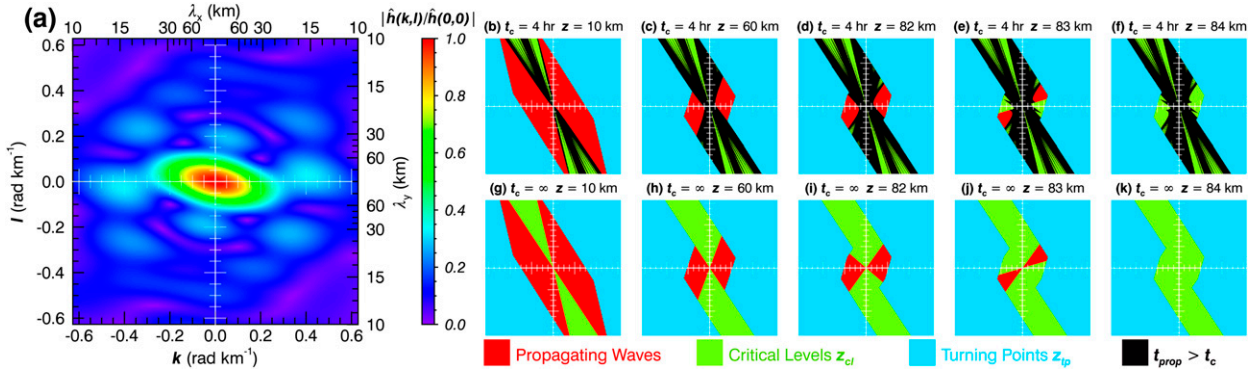

FIG. 10. (a) Normalized spectral terrain amplitude $|\tilde{h}(k, l)|/|\tilde{h}(0, 0)|$ for k and l in the range $\pm 2\pi$ $(10\,\text{km})^{-1}$. (b)–(k) Same region of spectral space, with colors representing propagation status by wavenumber of the Fourier solutions at 0600 UTC at altitudes z of (left)–(right) 10, 60, 82, 83, and 84 km. Red regions contain propagating waves. In all other regions, waves have been removed owing to critical levels (green), turning points (blue), or exceeding the cutoff time t_c for wave propagation (black). Results for (top) $t_c = 4$ h solutions and (bottom) $t_c = \infty$ (steady state) solutions.

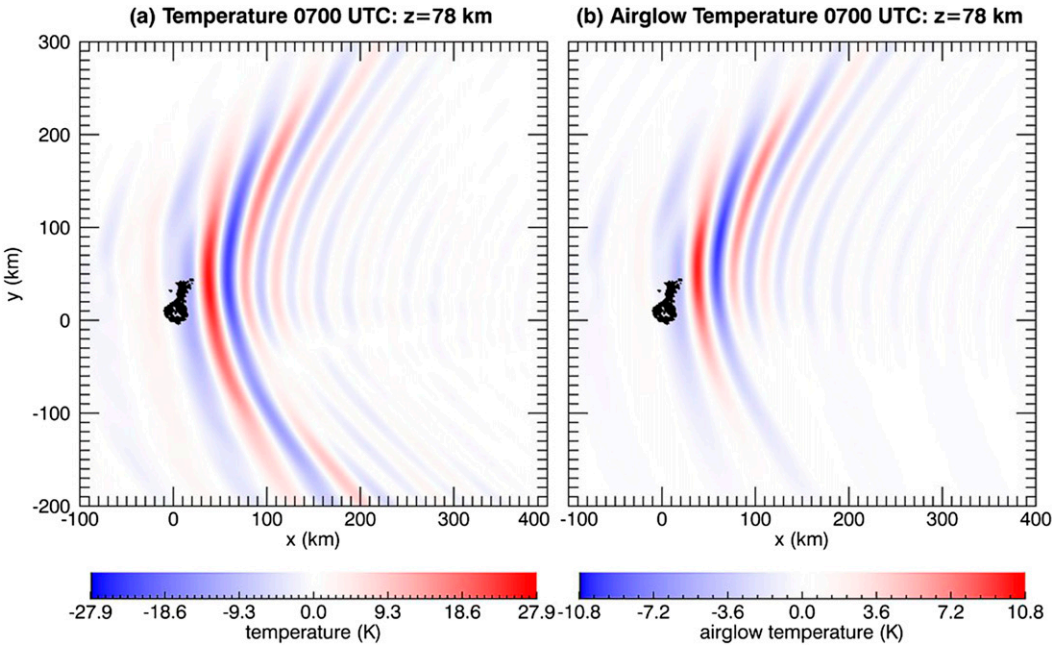

FIG. 11. (a) $T'(x, y, z, t_c)$ Fourier solution (K; color bar) at $z = 78$ km and $t_c = 4$ h, calculated using NAVGEM background profiles at 0700 UTC. (b) Modified solutions after applying the airglow filter function $S_{AG}(m)$ in (17) via (3).

As shown in Fig. 9, little filtering occurs from ~60 to 80 km, such that at $z = 82$ km (Figs. 10d and 10i) the regimes are largely unchanged from those at $z = 60$ km. By contrast, above 82 km the entire remaining propagation space is removed via critical levels within a 2-km vertical layer, so that at $z = 84$ km (Figs. 10f and 10k) not a single propagating harmonic remains. Again this result is in agreement with the observations in Fig. 6, which show large amplitudes at $z \sim 78$ km then rapid amplitude attenuation with height such that little or no wave activity is observed above 84 km. We also noted earlier that the steep forward face of the near-overturning wave crest at $z \sim 78$ and ~40 km east of the island terrain in Fig. 6 resembled tropospheric models of three-dimensional orographic gravity wave breaking below a zero-wind line (e.g., Miranda and Valente 1997). Our work confirms that this is in fact the case here: that is, that the outbound RF23 transect observed orographic gravity wave breaking just below a critical level in the MLT.

Next we conduct a detailed comparison of our Fourier solutions to the waves imaged in the airglow. Figure 11a shows the $T'(x, y, z, t_c)$ wave field after $t_c = 4$ h at $z = 78$ km, where solutions are still nearly linear and observed wave amplitudes in Fig. 6 peak. These solutions used the 0700 UTC NAVGEM profiles, which are closest in time to the outbound airglow measurements. Aspects of the modeled wave field show impressive quantitative agreement with the airglow imagery in Fig. 5, including (i) $\lambda_h \sim 40$ km waves downstream of the island, (ii) a cold phase line of longer λ_h immediately above the island, and (iii) a diverging wake of waves to the northeast. The nonhydrostatic dispersion relation (1) plays a pivotal role. The corresponding hydrostatic solution (not shown) has no $\lambda_h \sim 40$ km downstream waves: wave fields are concentrated near the island and in diverging wakes, have shorter λ_h and larger amplitudes, and become unstable at much lower altitudes. Thus, nonhydrostatic downstream group propagation and wave filtering at turning points exert first-order impacts on the observed MLT wave fields.

Aspects of Fig. 11a that differ from observed wave fields in Fig. 5a are (i) a diverging wake to the southeast that is not observed and (ii) peak amplitudes significantly larger than those in Fig. 5. One key aspect ignored to this point is the vertical averaging of the observed wave response via (15) due to the finite vertical width of the airglow emission profile $I(z)$. Since $I(z)$ extends to altitudes above 90 km, accurate numerical evaluation of (15) requires an accurate model of $T'(x, y, z', t_c)$ throughout the MLT, whereas our linear solutions begin to break down near 78 km (see Fig. 7). To gauge the effects more simply, we instead apply the spectral filter $S_{AG}(m)$ in (17) as an additional filter function multiplier S when inverting the Fourier solution $\tilde{T}(k, l, z)$ using (3) at $z = 78$ km for $t_c = 4$ h. The result is plotted in Fig. 11b. The two major discrepancies with the observations are largely eliminated: the southeastward diverging wake is now heavily suppressed in amplitude (since λ_z values

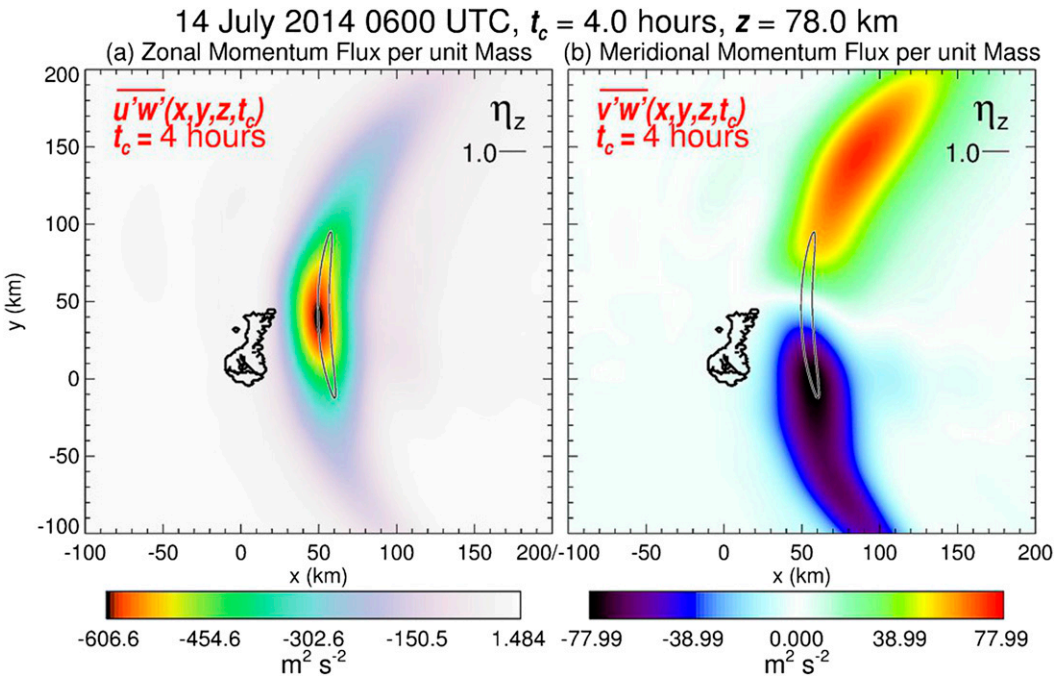

FIG. 12. 0600 UTC Fourier solutions for (a) $\overline{uw}(x, y, z, t_c)$ and (b) $\overline{vw}(x, y, z, t_c)$ (color bar and units beneath each panel) at $z = 78$ km and $t_c = 4$ h. Thin black contour shows regions of $\eta_z = 1$ in the corresponding steepness solution. Thick black contour shows coastline of Auckland Island.

here are short), and peak wave field amplitudes are now near the $\hat{T}_{AG} = 10$ K observed in Fig. 5b.

The vertical fluxes of zonal and meridional momentum per unit mass, $\overline{uw}(x, y, z, t_c)$ and $\overline{vw}(x, y, z, t_c)$ at $z = 78$ km after $t_c = 4$ h, are shown in Fig. 12 based on the 0600 UTC NAVGEM profiles. Gray lines show regions where $\eta_z > 1$ in the corresponding $\eta_z(x, y, z, t_c)$ wave field solution. Figure 12a exhibits strong concentration of zonal momentum flux ~40 km downstream of the mountain, with westward fluxes in the 300–600 m^2 s^{-2} range. These values are similar to (but somewhat larger than) the ~320 m^2 s^{-2} estimated by Pautet et al. (2016) using observed properties in Figs. 5b and 6 and linear gravity wave theory. Peak meridional fluxes in Fig. 12b are nearly an order of magnitude smaller and of roughly equal and opposite value in the northern and southern diverging wake regions, such that the area-averaged value is even smaller.

4. Temporal evolution of MLT winds and wave fields

a. *Semidiurnal tidal effects in the MLT*

Figure 13 shows hourly time series of analyzed wind vectors $\mathbf{V}(z)$ and zonal winds $U(z)$ in the MLT from ~70–100 km over Auckland Island during RF23. They reveal a zero-wind line at $z \sim 86$–87 km at 0400–0500 UTC that systematically descends over the following hours to ~80 km by 1000 UTC. Descending structure is also evident in buoyancy frequencies $N(z)$ (not shown).

This descending wind and temperature structure is produced by a large-amplitude migrating semidiurnal tide in the MLT reanalysis. A Hovmöller diagram of analyzed zonal and meridional winds at 0.015 hPa ($z \sim$ 75 km) and 50.4°S for a 5-day period centered on RF23 is shown in Fig. 14. RF23 is depicted as the segment of the white horizontal line at 166°E (longitude of Auckland Island) between the two vertical black lines depicting RF23 takeoff and landing times. The plot reveals a wavenumber-2 (migrating) semidiurnal tide in the MLT over Auckland Island with an amplitude in both the zonal and meridional components of ~20–30 m s^{-1}. As the tide propagates rapidly to the west, peak eastward tidal winds just before takeoff at ~0400–0500 UTC (see Fig. 4) are replaced by peak westward tidal winds nearer the end of the flight at ~1000–1100 UTC. Despite these tidal modulations, winds over Auckland Island remain eastward at this altitude throughout the flight.

Tidal phase varies in the vertical, as evident in Fig. 15, which shows the corresponding Hovmöller diagram at 0.0064 hPa ($z \sim 81$ km). Tidal wind amplitudes are even larger at this altitude and tidal phase noticeably leads in time relative to tidal phase at 75 km. This phase

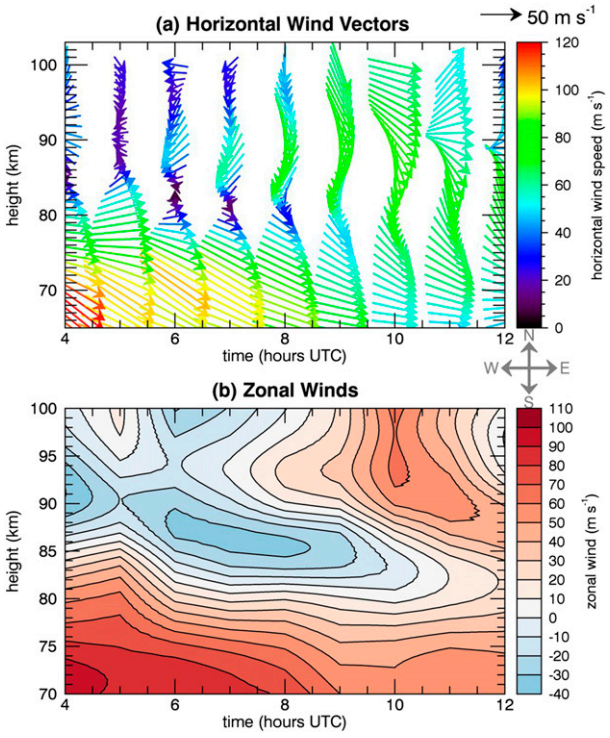

FIG. 13. (a) Horizontal wind vectors $\mathbf{V}(z)$ and (b) zonal-wind components $U(z)$ from NAVGEM reanalysis upstream of Auckland Island on 14 Jul 2014, plotted as function of time (hours UTC) from $z = 70$ to 100 km. Note weakening with time of mean easterlies at lower levels and descent with time of zero-zonal-wind line z_{u_0} [where $U(z_{u_0}) = 0$] due to migrating semidiurnal tide.

difference manifests locally above Auckland Island as phase descent of wind regimes with time as seen in Fig. 13. At takeoff zonal winds at 81 km in Fig. 15a are near the tidal node but are soon replaced by the tidal zonal-wind trough, causing $U(z)$ to transition from weakly eastward at the start of the flight at ~0600 UTC, to weakly westward by midflight at ~0900 UTC, then back to weakly eastward by landing time at ~1200 UTC.

Although there are no local MLT wind observations to validate these analyzed tides over Auckland Island, MLT winds have been measured at these latitudes using radars stationed in and around the southern tip of South America. Those measurements during previous austral winters revealed large-amplitude semidiurnal tidal winds with amplitudes of up to 80 m s^{-1} as well as weak diurnal tidal wind amplitudes (Fritts et al. 2010, 2012), consistent with the NAVGEM analyzed MLT wind fields over Auckland Island during RF23.

To summarize, a large-amplitude semidiurnal tide is responsible for descent of a zero-zonal-wind line over Auckland Island during RF23, from ~87 km just before takeoff to ~80 km just before landing, as shown in Fig. 13b.

b. Time–height evolution of wave fields

We computed η_z solutions from $z = 0$–100 km for t_c values ranging from 1 h to ∞ and for background profiles upstream of Auckland Island at all analysis times shown in Fig. 4 (0400–1200 UTC inclusive). As in section 3b, we used these to compute $\eta_z^{\max}(z, t_c)$ profiles via (21) and then used those to derive breaking heights z_b where $\eta_z^{\max}(z, t_c)$ first exceeds unity. The combined z_b results are shown in Fig. 16, revealing a secular decrease in z_b with time during RF23 in the wave field solutions over Auckland Island due to the influence on MLT wave propagation of the descending zero-zonal-wind line due to the semidiurnal tide (cf. Fig. 13b).

Figure 17 displays the time evolution of the $t_c = 4$ h wave field solutions in temperature $T'(x, y, z, t)$ and zonal momentum flux per unit mass $\overline{uw}(x, y, z, t)$ at $z =$ 78 km. Black contours overlay regions of the corresponding $\eta_z(x, y, z, t)$ solution that exceed unity, identifying regions where wave breaking is likely. At 0400 UTC, around 2 h prior to NGV takeoff, the wave fields at $z = 78$ km are stable with peak temperature amplitudes and zonal momentum fluxes per unit mass of ~20 K and -400 m^2 s^{-2}, respectively. Two hours later at 0600 UTC, these peak values have increased, such that a small unstable ($\eta_z > 1$) region forms ~40 km east of the island. This unstable region intensifies by 0800 UTC and migrates into the southeastern wing of the wave field. By 1000 UTC intense wave breaking is predicted throughout the eastern and southeastern regions of the wave field: only the northeastern wing remains stable.

5. Inbound NGV flight legs

a. Observations

Immediately after the first transect of Auckland Island at 0700 UTC, the NGV flew south to Macquarie Island, returning to Auckland Island at a lower flight altitude ~3 h later. As shown in Fig. 3, three additional transects of Auckland Island were performed during these inbound flight legs in an ascending "stair step" pattern.

Figure 18 shows the AMTM airglow and temperature imagery acquired during each of these transects. Much of the MLT wave structure seen at 0700 UTC in Fig. 5 is still evident at 1000 UTC (Figs. 18a and 18d), but wave amplitudes are weaker. For the subsequent overpass at ~1030 UTC (Figs. 18b and 18e), wave structure immediately downstream of the island has now disappeared, owing presumably to further breakdown of waves into turbulence. However waves in the diverging wake to the northeast are still present in the wing camera imagery. By ~1115 UTC (Fig. 18d) nearly all wave structure has

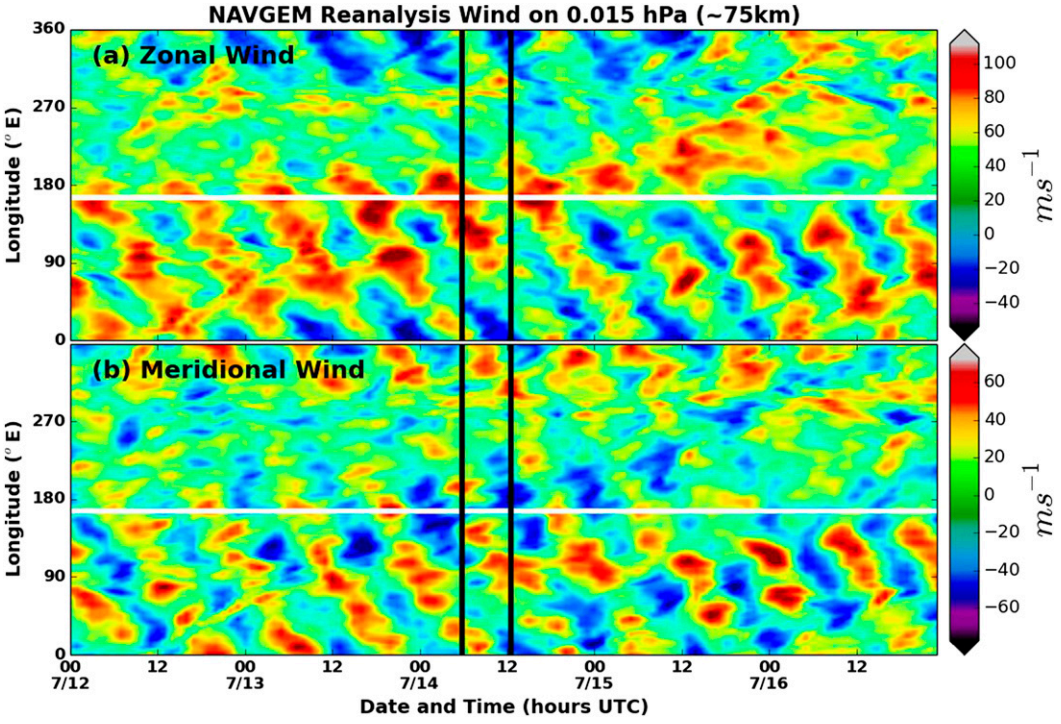

FIG. 14. Hovmöller plots of (a) zonal and (b) meridional winds at 0.015 hPa ($z \sim 75$ km) and 50.4°S from the NAVGEM reanalysis. Color bar wind scales at far right. Longitude of Auckland Island is shown by white horizontal line and black vertical lines show RF23 takeoff and landing times.

disappeared, with northeastern wave structure weakly visible but showing evidence of breakdown into smaller-scale instability structures. Correlative Na lidar observations were not available for these inbound transects.

b. *Fourier solutions*

The 1000 UTC wave field in Fig. 17d predicts intense wave breaking throughout the eastward and southeastward regions of the wave field, consistent with wave breakdown observed in these regions in Fig. 18. The surviving portion of the wave field is confined to the northeast in the wing camera imagery of Fig. 18b. Likewise, the $T'(x, y, z, t_c)$ solution in Fig. 17d reveals wave structure to the northeast of similar appearance to that observed and no regions of diagnosed wave breaking ($\eta_z \geq 1$) either.

As for the outbound data, a more quantitative comparison with the inbound AMTM data requires vertical integration of the wave response through the airglow emission layer $I(z)$. Figure 19b shows the 1000 UTC solution after applying the spectral airglow filter $S_{AG}(m)$ as before, revealing wave structure concentrated in the northeast quadrant of very similar appearance to that observed. Inferred amplitudes cannot be compared since temperatures are not retrieved from the wing camera observations.

To understand how filtering controls these changes in the MLT wave field structure at these later observation times, Fig. 20 shows propagating and filtered waves within the (k, l) spectral solution space at various heights in the MLT for solutions using the 0900 UTC analysis profiles. The region of propagating waves at $z = 76$ km is similar to that seen at ~0600 UTC (e.g., Fig. 10c). However, strong filtering of this propagating region occurs at lower MLT heights than at 0600 UTC owing to descending westward shear and zero-zonal-wind lines due to the semidiurnal tide (Fig. 13b), which in this case do not completely remove all propagating waves. Instead a narrow wedge of propagating waves with **k** vectors aligned northwest/southeast remains at $z = 84$ km and above (Figs. 20c and 20f). This transmission is facilitated by stronger southward meridional MLT winds at this time, which prevent complete stagnation of the vector wind. It is these surviving waves that produce the wave activity to the northeast both observed in Figs. 18a and 18b and reproduced in the Fourier solutions in Fig. 19b.

6. Discussion and conclusions

MLT airglow imagery acquired during NGV transects of Auckland Island during DEEPWAVE RF23 (Figs. 5

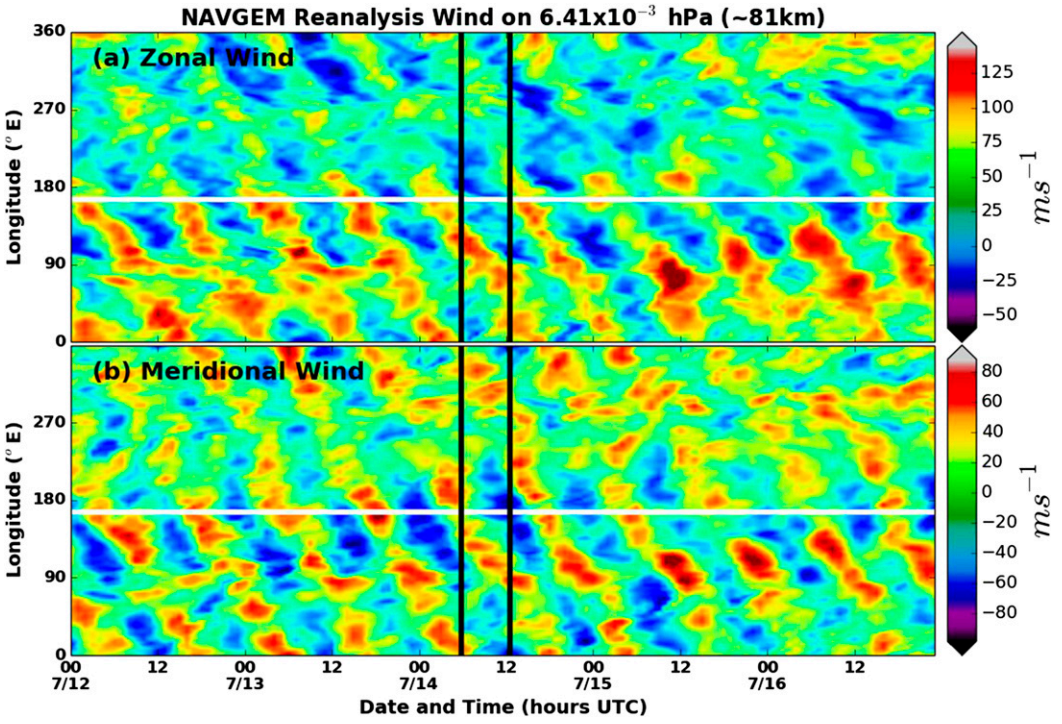

FIG. 15. As in Fig. 14, but at 0.0064 hPa ($z \sim 81$ km) and 50.4°S. Note also change in dynamical range of color bars relative to Fig. 14.

and 18) appear to reveal a three-dimensional orographic gravity wave response to flow over island terrain at unexpectedly high altitudes (Fritts et al. 2016; Pautet et al. 2016). The present work has thoroughly investigated the dynamics of this event from the ground to the MLT. We showed that the upstream flow impinging on Auckland Island terrain satisfied conditions for linear surface forcing (Fr $\gg 1$). Our ensuing linear Fourier solutions, derived using analyzed upstream wind, temperature, stability, and density profiles and realistic island terrain, remained stable (i.e., linear: $\eta_z < 1$) at all points in the wave field up to $z \sim$70–80 km (see Fig. 16). Beyond merely establishing the validity of linear approximations over this deep vertical layer of the atmosphere, our linear solutions accurately reproduced (and provided explanations for) all the salient observed features of these MLT wave fields—wave-breaking heights, time evolution of three-dimensional wave field structure, downstream horizontal wavelengths, airglow temperature amplitudes, lidar-derived vertical displacement amplitudes, and inferred momentum fluxes per unit mass. In summary, we can now confidently classify this observed event as a remarkable validated case study of three-dimensional nonhydrostatic orographic gravity waves from an island evolving linearly from the surface to very high altitudes right up to the point of observed incipient wave breaking in the MLT.

Why do we find linear orographic gravity waves up to the MLT to be remarkable? Linear hydrostatic wave equations are used routinely to parameterize subgrid-scale orographic gravity wave breaking and drag within NWP and climate models [see, e.g., section 2a of Eckermann et al. (2015b)]. In the absence of shear, those equations yield wave amplitude increases with height of

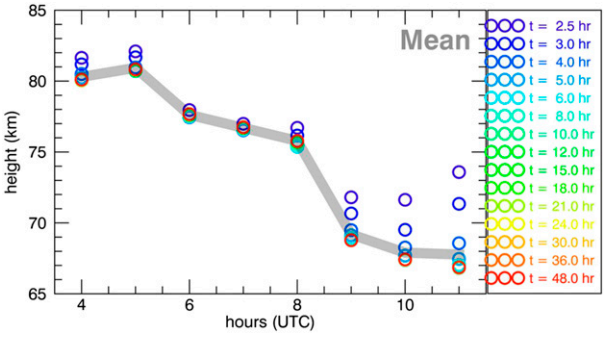

FIG. 16. Breaking heights z_b as a function of time (UTC hours on 14 Jul 2014) derived by identifying the height z where Fourier wave field solutions $\eta_z(x, y, z, t_c)$ over Auckland Island first exceed unity. Gray curve shows mean z_b computed over all t_c values at a given universal time.

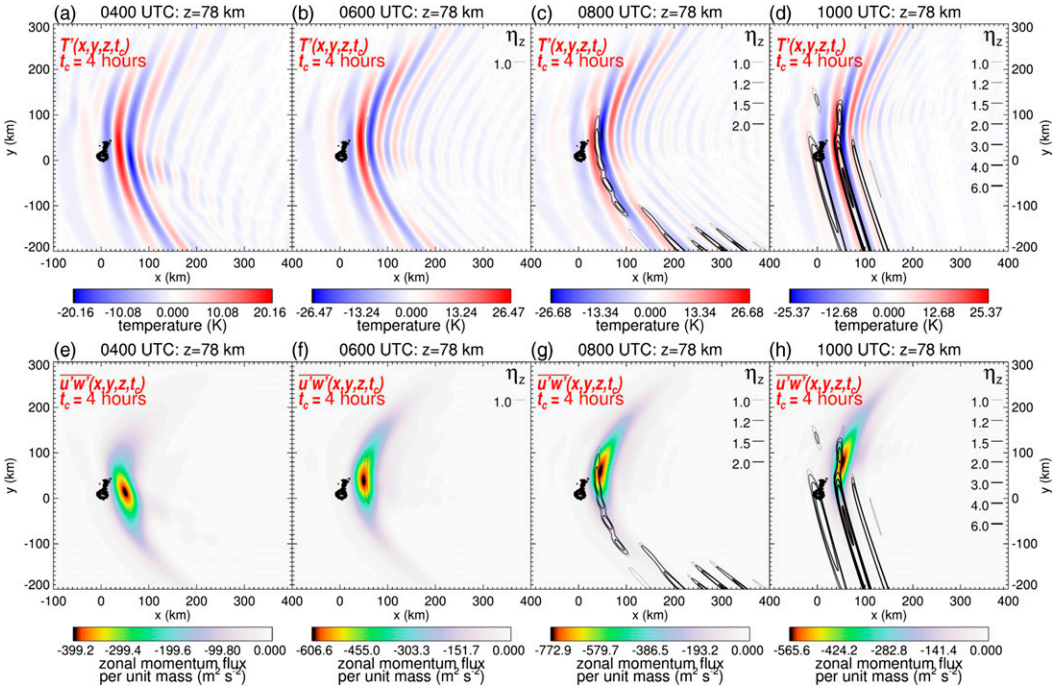

FIG. 17. Fourier wave field solutions for (a)–(d) temperature perturbations $T'(x, y, z, t_c)$ and (e)–(h) vertical fluxes of zonal momentum per unit mass $\overline{uw}(x, y, z, t_c)$, at $z = 78$ km and $t_c = 4$ h, based on upstream reanalysis profiles at (left)–(right) 0400, 0600, 0800, and 1000 UTC. Auckland Island is shaded. Unstable regions of the wave fields are highlighted by black contours, showing $\eta_z \geq 1$ regions of the corresponding steepness solutions $\eta_z(x, y, z, t_c)$: see η_z contour legend at top right of each panel.

$d(z) = [\rho_0/\rho(z)]^{1/2}$. At $z \sim 78$ km, where our observations and modeling indicate RF23 wave fields first break (Fig. 6), $d(z) = 300$, so that, for a representative surface wave amplitude of $\hat{\eta}_0 = 500$ m (Fig. 1), an amplitude $d(z)\hat{\eta}_0 \sim 150$ km at $z = 78$ km would be predicted. This unrealistically large value implies $z_b \ll 78$ km, and indeed parameterized midlatitude orographic gravity wave breaking typically occurs first in the troposphere or lower stratosphere (e.g., McFarlane 1987).

So what processes operate here to keep wave fields linear up to such unexpectedly high altitudes? At least three stabilizing dynamical effects are important in our Fourier solutions. First, refraction by background winds affects wave amplitudes via the spectral $g(k, l, z)$ term [(5)], which, in the hydrostatic limit for purely zonal winds $U(z)$ and constant N, reduces to a height profile $g(z) = [U(0)/U(z)]^{1/2}$. The change in $U(z)$ from $\sim$20 m s^{-1} at the surface to $\sim$100 m s^{-1} at $z \sim 55$ km (see Fig. 4) reduces amplitudes by a factor $g(z) \sim 0.45$ over this altitude range. Second, the horizontal spreading of wave fields into progressively larger horizontal areas away from Auckland Island (e.g., Figs. 17a–17d) leads to corresponding decreases in local wave field amplitudes to conserve wave action (Eckermann et al. 2015b,a; Broutman et al. 2016, manuscript submitted to *J. Geophys. Res.*). Finally, the progressive erosion with height of amplitude contributions at specific harmonics (k, l) via directional critical levels and turning points (e.g., Figs. 9 and 10) further reduces the vertical growth of local wave field amplitudes with height. These three processes acting together allow linear conditions to persist deep into the mesosphere. Nonhydrostatic effects, specifically downstream group propagation accompanied by enhanced horizontal geometrical spreading (Broutman et al. 2016, manuscript submitted to *J. Geophys. Res.*) and turning-point filtering have large impacts on our linear solutions, but are typically not included in orographic gravity wave drag parameterizations in NWP and climate models.

A potential weakness of our Fourier solutions is in our treatment of time dependence, which involves imposition of propagation cutoffs t_c to the steady-state Fourier solutions. Solutions initialized at 0400 UTC, for example, can be visualized as waves emanating from the bottom-left corner of Fig. 4 as many oblique ray paths for each (k, l), each meandering upward and to the right through this (z, t) space. Although our spectral t_c cutoff incorporates this group propagation,

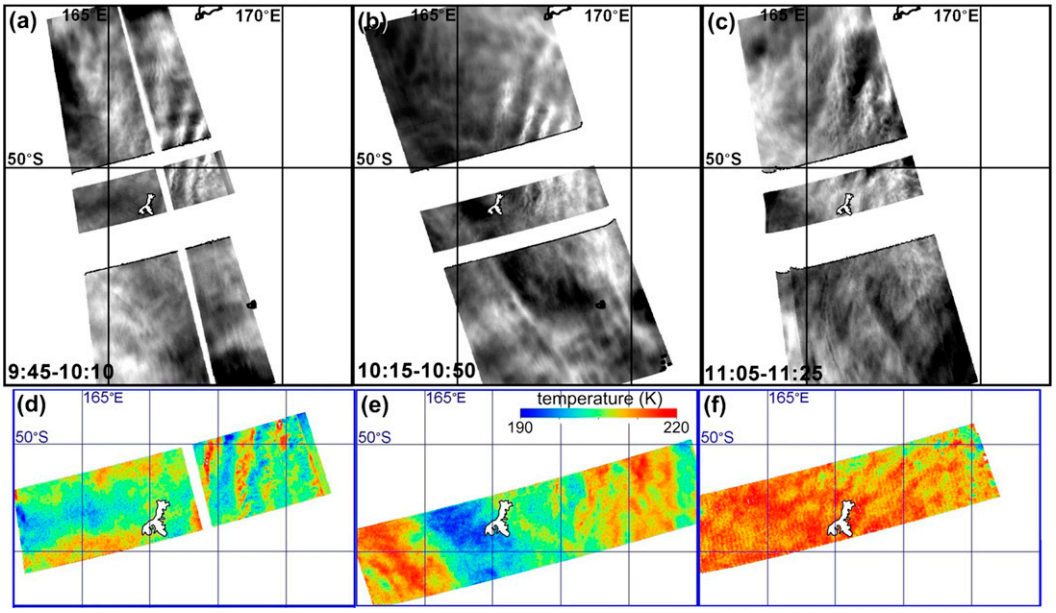

FIG. 18. Presentation of AMTM (a)–(c) airglow and (d)–(f) temperature imagery as in Fig. 5, but showing results for Auckland Island transects from (left) 0945–1010, (center) 1015–1050, and (right) 1105–1125 UTC.

our solutions do not account for the time-varying wind fields that each wave group encounters in Fig. 4 as it propagates forward in time. Instead, our solutions assume the wind profile at initialization ($t = 0$) remains the same.

The effects of time-dependent winds on linear wave fields can be gauged using a ray equation that, after simplifying here to zonally aligned winds and waves and ignoring horizontal gradients so that k remains constant, can be expressed as

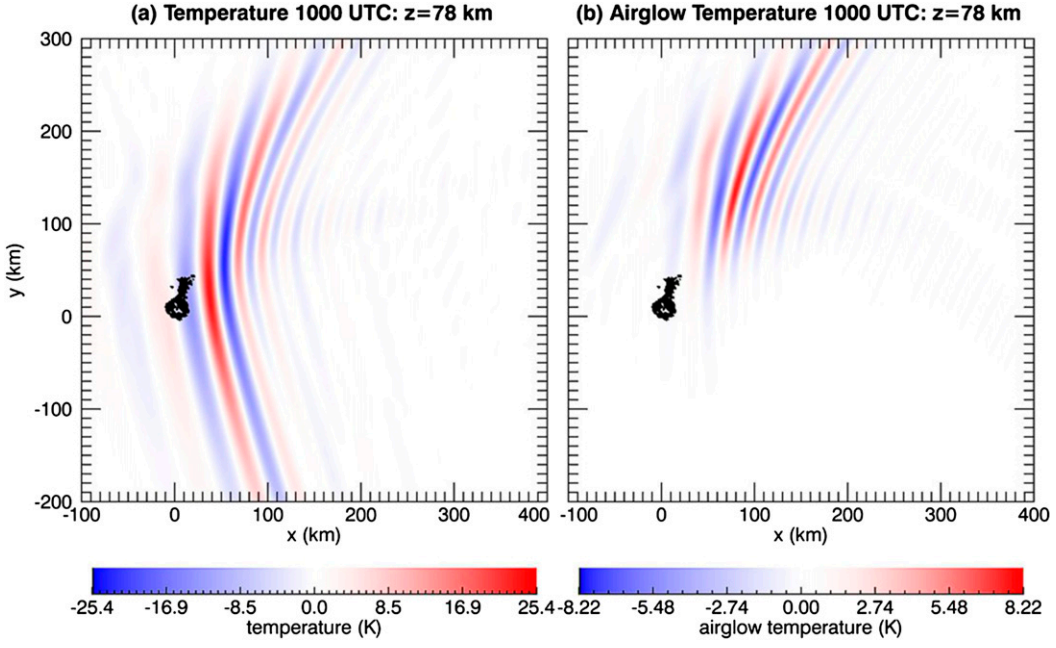

FIG. 19. Temperature perturbation presentation as in Fig. 11, but for the 1000 UTC Fourier solutions ($t_c = 4$ h) at $z = 78$ km.

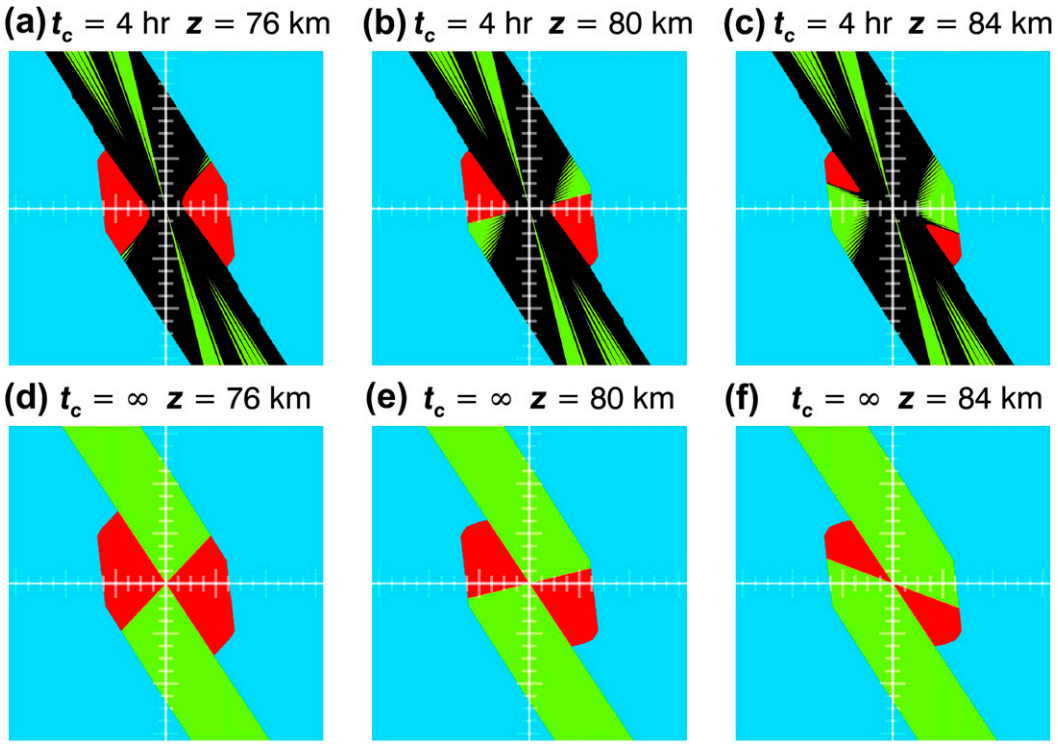

FIG. 20. Regions of (k, l) space within the $\pm 2\pi$ $(10\,\text{km})^{-1}$ range, as in Fig. 10, but here depicting the Fourier solutions at 0900 UTC at z = (left) 76, (center) 80, and (right) 84 km. Propagating waves are shown in red. All other regions contain nonpropagating waves owing to prior removal by critical levels (green), turning points (blue), or exceeding the time limit t_c for wave propagation (black). Results for (a)–(c) the t_c = 4-h solutions and (d)–(f) the $t_c = \infty$ (steady state) solutions.

$$c(t) = c_0 + \frac{\partial U}{\partial t}\Delta t. \tag{22}$$

Here c is zonal phase speed along a ray path, which we assume to be initially stationary ($c_0 = 0$). In the MLT, semidiurnal wind amplitudes range from ~20 to 50 m s^{-1} (Figs. 14 and 15) so $|\partial U/\partial t|$ can be large locally, potentially accelerating c and affecting when and where waves break (e.g., Eckermann and Marks 1996). The issue here comes down to the wave propagation time Δt in (22), which we estimate as the time required to propagate from z = 60 km, where tidal amplitudes first become significant, to z = 78 km where waves initially break: we evaluate Δt using (7) with the above height integration limits. Representative calculations for the $\lambda_h \sim 40$ km waves to the east of Auckland Island using reanalysis winds yield $\Delta t \sim$ 10–20 min. So, notwithstanding large $|\partial U/\partial t|$, waves propagate so rapidly through MLT tidal winds that little change in c occurs via (22), explaining why our Fourier solutions that omit such effects compare so closely to observations. That said, waves in the southeastern diverging wake propagate more slowly in the vertical and might be affected more by tidal accelerations, including tidal $\partial V/\partial t$ accelerations.

We conclude by estimating effects on the MLT of the local deposition of these wave field momentum and energy fluxes through wave breaking. Irreversible flow accelerations due to wave momentum flux deposition are given by

$$\frac{\partial U}{\partial t} = a(z) = -\frac{1}{\rho}\frac{\partial}{\partial z}(\rho\overline{uw}). \tag{23}$$

Since our Fourier solutions do not model wave breaking, here we perform a separate calculation. We specify a stationary ($c = 0$) wave field at z = 78 km (just prior to wave breaking) of λ_h = 40 km and $\overline{uw} = -300\,\text{m}^2\,\text{s}^{-2}$, values derived directly from observations by Pautet et al. (2016), who noted that these fluxes are ~10–100 times larger than typical $\overline{uw}$ values observed in the MLT. Our model results in Figs. 12a and 17h–17k reproduce similar or larger local flux values. We use linear saturation theory (e.g., Holton 1983; McFarlane 1987) to model breaking and deposition of these fluxes through analyzed 0600 UTC zonal winds, which, as shown in Fig. 21a,

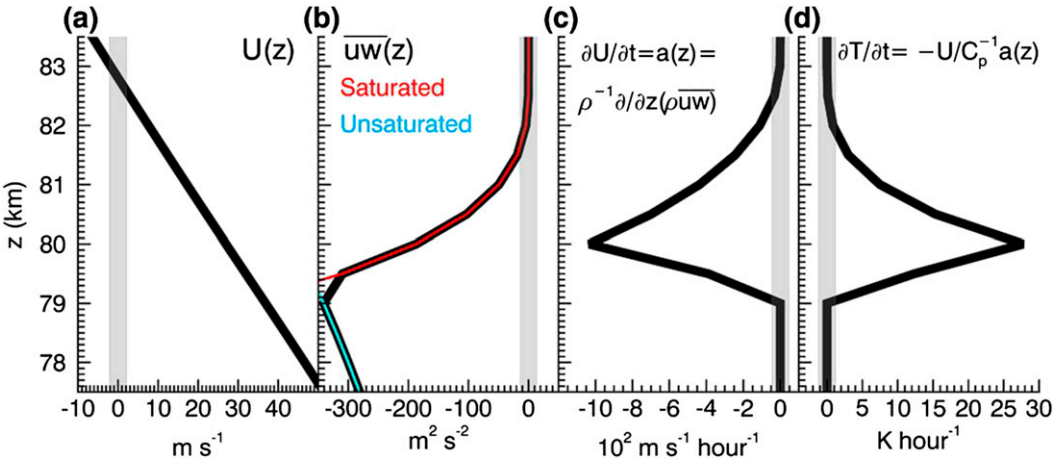

FIG. 21. Profiles from $z \sim 78$ to 83 km of (a) 0600 UTC reanalysis zonal winds $U(z)$ and linear saturation calculations of wave-induced (b) momentum flux per unit mass, (c) flow accelerations $a(z)$, and (d) dynamical heating rates $H_1(z)$. Gray lines show zero values. See text for further details.

decrease with height to a critical level at $z \sim 83$ km. These decreasing winds cause all the wave momentum flux to be deposited within a narrow vertical layer beneath this zero-wind line (see Fig. 21b), largely consistent with the rapid attenuation with height of wave amplitudes above 78 km evident in the lidar data in Fig. 6. This results in huge flow accelerations in Fig. 21c, with a density-weighted layer-averaged value from $z \sim 79$ to 83 km of around $-350\,\mathrm{m\,s^{-1}\,h^{-1}}$. Such intense localized forcing likely triggers an intense surrounding ageostrophic circulation and secondary wave generation. This would imply a remarkably rapid evolution from linear wave field dynamics to strongly nonlinear local dynamics due to rapid and intense wave breaking beneath a critical level.

Corresponding dynamical heating rates are given by

$$\frac{\partial T}{\partial t} = -\frac{U}{C_p}a + \frac{T}{(1+\mathrm{Pr})}\frac{\partial}{\partial p}(U\rho a) \tag{24}$$

$$= H_1(z) + H_2(z), \tag{25}$$

where p is pressure and C_p is mass specific heat at constant pressure (Medvedev and Klaassen 2003). The quantity $H_2(z)$ is a differential heating term due to the wave's vertical heat-flux divergence. We neglect it here since its form depends sensitively on assumption about wavebreaking dynamics [e.g., effective Prandtl numbers (Pr) Akmaev 2007] and on the vertical curvature of the momentum flux profile, which the simple calculations here do not accurately constrain. Furthermore, the density-weighted layer average of $H_2(z)$ vanishes (Medvedev and Klaassen 2003).

The heating rates $H_1(z)$ due to frictional dissipation of total wave energy density, plotted in Fig. 21d, are large, with a corresponding density-weighted layer average from $z \sim 79$ to 83 km of $\sim 8\,\mathrm{K\,h^{-1}}$. Figures 18d–18f provide possible observational support for these large inferred heating rates, with mean temperatures averaged through the airglow layer increasing by ~10–15 K over the ~1–1.5 h of measurements during three separate NGV transects, when these waves are observed to be breaking vigorously and depositing their energy and momentum locally in the MLT.

Since such large upper-level MLT drag will also significantly affect deep underlying atmospheric layers through downward control [see, e.g., Garcia and Boville (1994)], the above calculations provide direct observational support for recent conjectures that orographic gravity wave drag due to subantarctic islands contributes significantly to the overall momentum and energy budget controlling the middle-atmospheric circulation and climate during austral winter (Alexander et al. 2009; McLandress et al. 2012).

Acknowledgments. NGV MLT instruments were funded by NSF Grants AGS-1061892 (USU) and AGS-1261619 (GATS). Scientific contributions were funded by NSF Grants AGS-1338557 (DB and JM), AGS-1338666 (PDP and MJT), AGS-1338646 (KB, BPW, and DCF), and AGS-1338655 (RBS). SDE and JDD acknowledge generous support of the Chief of Naval Research via the base 6.1 and platform support programs (PE-61153N). RF23 is a testament to the dedication and flight-planning skills of the entire DEEPWAVE mission team: particular thanks go to Jim Doyle and Pavel Romashkin as the NGV mission scientist and flight manager, respectively, for RF23. The authors acknowledge support of the DEEPWAVE Data Archive Center at NCAR's Earth Observing

Laboratory (https://www.eol.ucar.edu/field_projects/deepwave/). The NAVGEM reanalyses were facilitated by the DoD High Performance Computer Modernization Program via grants of computer time at the Navy DoD Supercomputing Resource Center. The ASTER global digital elevation model version 2 (GDEM V2) is a product of METI (Ministry of Economy, Trade and Industry, Japan) and NASA.

REFERENCES

Akmaev, R. A., 2007: On the energetics of mean-flow interactions with thermally dissipating gravity waves. *J. Geophys. Res.*, **112**, D11125, doi:10.1029/2006JD007908.

Alexander, M. J., and A. W. Grimsdell, 2013: Seasonal cycle of orographic gravity wave occurrence above small islands in the Southern Hemisphere: Implications for effects on the general circulation. *J. Geophys. Res. Atmos.*, **118**, 11 589–11 599, doi:10.1002/2013JD020526.

——, S. D. Eckermann, D. Broutman, and J. Ma, 2009: Momentum flux estimates for South Georgia Island mountain waves in the stratosphere observed via satellite. *Geophys. Res. Lett.*, **36**, L12816, doi:10.1029/2009GL038587.

Andreassen, Ø., P. Ø. Hvidsten, D. C. Fritts, and S. Arendt, 1998: Vorticity dynamics in a breaking internal gravity wave. Part 1. Initial instability evolution. *J. Fluid Mech.*, **367**, 27–46, doi:10.1017/S0022112098001645.

Bossert, K., and Coauthors, 2015: Momentum flux estimates accompanying multiscale gravity waves over Mount Cook, New Zealand, on 13 July 2014 during the DEEPWAVE campaign. *J. Geophys. Res. Atmos.*, **120**, 9323–9337, doi:10.1002/2015JD023197.

Broutman, D., J. Ma, S. D. Eckermann, and J. Lindeman, 2006: Fourier-ray modeling of transient trapped lee waves. *Mon. Wea. Rev.*, **134**, 2849–2856, doi:10.1175/MWR3232.1.

——, S. D. Eckermann, and J. W. Rottman, 2009: Practical application of two turning-point theory to mountain-wave transmission through a wind jet. *J. Atmos. Sci.*, **66**, 481–494, doi:10.1175/2008JAS2786.1.

Butchart, N., and Coauthors, 2011: Multimodel climate and variability of the stratosphere. *J. Geophys. Res.*, **116**, D05102, doi:10.1029/2010JD014995.

Doyle, J. D., Q. Jiang, R. B. Smith, and V. Grubišić, 2011: Three-dimensional characteristics of stratospheric mountain waves during T-REX. *Mon. Wea. Rev.*, **139**, 3–23, doi:10.1175/2010MWR3466.1.

Eckermann, S. D., and C. J. Marks, 1996: An idealized ray model of gravity wave-tidal interactions. *J. Geophys. Res.*, **101**, 21 195–21 212, doi:10.1029/96JD01660.

——, and D. L. Wu, 2012: Satellite detection of orographic gravity-wave activity in the winter subtropical stratosphere over Australia and Africa. *Geophys. Res. Lett.*, **39**, L21807, doi:10.1029/2012GL053791.

——, D. E. Gibson-Wilde, and J. T. Bacmeister, 1998: Gravity wave perturbations of minor constituents: A parcel advection methodology. *J. Atmos. Sci.*, **55**, 3521–3539, doi:10.1175/1520-0469(1998)055<3521:GWPOMC>2.0.CO;2.

——, D. Broutman, and J. Lindeman, 2006a: Fourier-ray modeling of short-wavelength trapped lee waves observed in infrared satellite imagery near Jan Mayen. *Mon. Wea. Rev.*, **134**, 2830–2848, doi:10.1175/MWR3218.1.

——, A. Dörnbrack, S. B. Vosper, H. Flentje, M. J. Mahoney, T. P. Bui, and K. S. Carslaw, 2006b: Mountain wave-induced polar stratospheric cloud forecasts for aircraft science flights during SOLVE/THESEO 2000. *Wea. Forecasting*, **21**, 42–68, doi:10.1175/WAF901.1.

——, and Coauthors, 2009: High-altitude data assimilation system experiments for the northern summer mesosphere season of 2007. *J. Atmos. Sol.-Terr. Phys.*, **71**, 531–551, doi:10.1016/j.jastp.2008.09.036.

——, J. Lindeman, D. Broutman, J. Ma, and Z. Boybeyi, 2010: Momentum fluxes of gravity waves generated by variable Froude number flow over three-dimensional obstacles. *J. Atmos. Sci.*, **67**, 2260–2278, doi:10.1175/2010JAS3375.1.

——, D. Broutman, and H. Knight, 2015a: Effects of horizontal geometrical spreading on the parameterization of orographic gravity wave drag. Part II: Analytical solutions. *J. Atmos. Sci.*, **72**, 2348–2365, doi:10.1175/JAS-D-14-0148.1.

——, J. Ma, and D. Broutman, 2015b: Effects of horizontal geometrical spreading on the parameterization of orographic gravity wave drag. Part I: Numerical transform solutions. *J. Atmos. Sci.*, **72**, 2330–2347, doi:10.1175/JAS-D-14-0147.1.

Fritts, D. C., and Coauthors, 2010: Southern Argentina Agile Meteor Radar: System design and initial measurements of large-scale winds and tides. *J. Geophys. Res.*, **115**, D18112, doi:10.1029/2010JD013850.

——, D. Janches, H. Iimura, W. K. Hocking, J. V. Bageston, and N. M. P. Leme, 2012: Drake Antarctic Agile Meteor Radar first results: Configuration and comparison of mean and tidal wind and gravity wave momentum flux measurements with Southern Argentina Agile Meteor Radar. *J. Geophys. Res.*, **117**, D02105, doi:10.1029/2011JD016651.

——, and Coauthors, 2014: Quantifying gravity wave momentum fluxes with mesosphere temperature mappers and correlative instrumentation. *J. Geophys. Res. Atmos.*, **119**, 13 583–13 603, doi:10.1002/2014JD022150.

——, and Coauthors, 2016: The Deep Propagating Gravity Wave Experiment (DEEPWAVE): An airborne and ground-based exploration of gravity wave propagation and effects from their sources throughout the lower and middle atmosphere. *Bull. Amer. Meteor. Soc.*, **97**, 425–453, doi:10.1175/BAMS-D-14-00269.1.

Garcia, R. R., and B. A. Boville, 1994: Downward control of the mean meridional circulation and temperature distribution of the polar winter stratosphere. *J. Atmos. Sci.*, **51**, 2238–2245, doi:10.1175/1520-0469(1994)051<2238:COTMMC>2.0.CO;2.

Hodur, R. M., 1997: The Naval Research Laboratory's Coupled Ocean/Atmosphere Mesoscale Prediction System (COAMPS). *Mon. Wea. Rev.*, **125**, 1414–1430, doi:10.1175/1520-0493(1997)125<1414:TNRLSC>2.0.CO;2.

Hogan, T. F., and Coauthors, 2014: The Navy Global Environmental Model. *Oceanography*, **27**, 116–125, doi:10.5670/oceanog.2014.73.

Holton, J. R., 1983: The influence of gravity wave breaking on the general circulation of the middle atmosphere. *J. Atmos. Sci.*, **40**, 2497–2507, doi:10.1175/1520-0469(1983)040<2497:TIOGWB>2.0.CO;2.

Hoppel, K. W., S. D. Eckermann, L. Coy, G. E. Nedoluha, D. R. Allen, S. D. Swadley, and N. L. Baker, 2013: Evaluation of SSMIS upper atmosphere sounding channels for high-altitude data assimilation. *Mon. Wea. Rev.*, **141**, 3314–3330, doi:10.1175/MWR-D-13-00003.1.

Jiang, Q., A. Reinecke, and J. D. Doyle, 2014: Orographic wave drag over the Southern Ocean: A linear perspective. *J. Atmos. Sci.*, **71**, 4235–4252, doi:10.1175/JAS-D-14-0035.1.

Laursen, K. K., D. P. Jorgensen, G. P. Brasseur, S. L. Ustin, and J. R. Huning, 2006: HIAPER: The next generation NSF/NCAR research aircraft. *Bull. Amer. Meteor. Soc.*, **87**, 896–909, doi:10.1175/BAMS-87-7-896.

Liu, A. Z., and G. R. Swenson, 2003: A modeling study of O_2 and OH airglow perturbations induced by atmospheric gravity waves. *J. Geophys. Res.*, **108**, 4151, doi:10.1029/2002JD002474.

McFarlane, N. A., 1987: The effect of orographically excited gravity wave drag on the general circulation of the lower stratosphere and troposphere. *J. Atmos. Sci.*, **44**, 1775–1800, doi:10.1175/1520-0469(1987)044<1775:TEOOEG>2.0.CO;2.

McLandress, C., T. G. Shepherd, S. Polavarapu, and S. R. Beagley, 2012: Is missing orographic gravity wave drag near 60°S the cause of the stratospheric zonal wind biases in chemistry climate models? *J. Atmos. Sci.*, **69**, 802–818, doi:10.1175/JAS-D-11-0159.1.

Medvedev, A. S., and G. P. Klaassen, 2003: Thermal effects of saturating gravity waves in the atmosphere. *J. Geophys. Res.*, **108**, 4040, doi:10.1029/2002JD002504.

Miranda, P. M. A., and M. A. Valente, 1997: Critical level resonance in three-dimensional flow past isolated mountains. *J. Atmos. Sci.*, **54**, 1574–1588, doi:10.1175/1520-0469(1997)054<1574:CLRITD>2.0.CO;2.

Pautet, P.-D., M. J. Taylor, W. R. Pendleton Jr., Y. Zhao, T. Yuan, R. Esplin, and D. McLain, 2014: Advanced mesospheric temperature mapper for high-latitude airglow studies. *Appl. Opt.*, **53**, 5934–5943, doi:10.1364/AO.53.005934.

——, and Coauthors, 2016: Large amplitude mesospheric response to an orographic wave generated over the Southern Ocean Auckland Islands (50.7°S) during the DEEPWAVE project. *J. Geophys. Res. Atmos.*, **121**, 1431–1441, doi:10.1002/2015JD024336.

Reinecke, P. A., and D. R. Durran, 2008: Estimating topographic blocking using a Froude number when the static stability is nonuniform. *J. Atmos. Sci.*, **65**, 1035–1048, doi:10.1175/2007JAS2100.1.

Smith, R. B., 1989: Mountain-induced stagnation points in hydrostatic flow. *Tellus*, **41A**, 270–274, doi:10.1111/j.1600-0870.1989.tb00381.x.

Vosper, S. B., 2015: Mountain waves and wakes generated by South Georgia: Implications for drag parametrization. *Quart. J. Roy. Meteor. Soc.*, **141**, 2813–2827, doi:10.1002/qj.2566.

Xu, J., A. K. Smith, R. L. Collins, and C.-Y. She, 2006: Signature of an overturning gravity wave in the mesospheric sodium layer: Comparison of a nonlinear photochemical-dynamical model and lidar observations. *J. Geophys. Res.*, **111**, D17301, doi:10.1029/2005JD006749.

Young, K., T. Hock, and C. Martin, 2014: NSF/NCAR GV HIAPER QC dropsonde data, version 3.0. UCAR Earth Observing Laboratory, accessed 4 December 2015, doi:10.5065/D6XW4GTB.